Investigation of Passivating Layers in c-Si Solar Cells Using a Corona Charging System

Master of Science Thesis

Riqian Liu

TUDelft Delft University of Technology

Investigation of Passivating Layers in c-Si Solar Cells Using a Corona Charging System

Master of Science Thesis

by

Riqian Liu

in partial fulfillment of the requirements for the degree of

Master of Science

in Electrical Sustainable Energy

Department of Photovoltaic Material and Device (PVMD)

Faculty of Electrical Engineering, Mathematics, and Computer Science (EEMCS)

Delft University of Technology

To be defended publicly on 26st July 2017 at 10:30 AM

Supervisors:	Prof.dr.ir. Miro Zeman
	Dr.ir. Olindo Isabella
	Dr.ir. Armando Rodrigo Mor
	Mr. Stefaan Heirman
Thesis Committee:	Prof.dr.ir Arno Smets
	Dr.ir. Olindo Isabella
	Dr.ir. Jianning Dong

TUDelft Delft University of Technology

Acknowledgement

First, I would like to express my gratitude to the staff of Delft Spectral Technologies: my daily supervisor Stefaan, who has been willing to help me no matter what kinds of problems I meet, making my ideas into a genuine product, teaching me a lot of things beyond the knowledge; Jimmy, always guiding me when I lost my directions, and helping me to solve scientific questions and helping me with the sample preparation; Remko, super software support, helping me adding any functions as required; Marc, although we do not meet much, you still help me with my presentations.

Secondly, I would like to thank the helpful colleagues and professors from PVMD group. Dr. Olindo Isabella provided the opportunity to me to do the research that has significantly raised my interest in the field of photovoltaics. Dimitris, although we do not meet at the beginning, you still give me lots of useful tips in both studying and daily life. Besides, Guangtao and Yue offered me samples to continue my experiments.

Thirdly, a special thank goes to my friends, Yan, Hao, Songsheng, Meng, Yuguang and many others. Thank you for providing all the moral and mental support to me and many valuable discussions that have considerably broaden my horizons. Being friends with you has been the greatest experience in my life, and I would like to give you my sincere appreciation.

My girlfriend Mingming, you are always my haven, I love you!

My thanks to my parents are always beyond words. During the three-year study, they have provided me incredible encouragement and support.

Riqian Liu

Delft, July 2017

Abstract

There are two existing surface passivation principles. Passivation of unsaturated Si bonds is called chemical passivation. Surface passivation can also be achieved by shielding the minority charge carriers from the semiconductor interface by means of an electric field. This method is referred to as field-effect passivation.

To test the effect of the field-effect passivation provided by the passivation layer, fixed charge density is the most important parameter. Delft Spectral Technologies (DST) developed a new Corona Charging System used to measure this value. It integrates the corona charging and Kelvin probe into one box. As the corona charging system is still in prototype, several improvements are made to the system, especially the improvements of the charge uniformity. In the thesis four different charging plans are compared to acquire the best charge uniformity.

Several passivation layers are tested with the DST corona charging system to measure their fixed charge density, including Atomic Layer Deposition (ALD) Al_2O_3, Plasma Enhanced Chemical Vapor Deposition (PECVD) SiN_x, Low Pressure Chemical Vapor Deposition (LPCVD) poly-Si. Morphology of the c-Si bulk influence on the fixed charge density in ALD Al_2O_3 has also been studied.

Finally, research on the charge decaying properties has been done, to find out the stability of the corona charges on different passivation layers.

Keywords: Field-effect passivation, Corona, Charge Uniformity, Fixed Charge Density

Table of Contents

List of Figures

List of Tables

List of Symbols

Name	Unit	Description
D_{it}	cm^{-2}V^{-1}	Density of interface traps
Q_f	cm^{-2}	Fixed charge density
S(SRV)	cm/s	Surface recombination velocity
Q_c	cm^{-2}	Corona charge density
Q_n	cm^{-2}	Net charge density
J_{0s}	fA/cm^2	surface saturation current density
U	kV	Voltage between the probe and the sample
ε_r	1	Relative electric permittivity
ε_0	F/m	Electric permittivity of vacuum
A	cm^2	Surface area of the probe
z	cm	Vibrating amplitude
d_0	cm	Distance between the probe and the sample
V_p	V	Voltage of the Kelvin Probe
ε_s	1	Relative electric permittivity of the sample
d_s	cm	Thickness of the sample
C_s	F	Capacitance of the sample
ω	Hz	Vibration frequency
D_p	cm^{2}s^{-1}	Diffusion coefficient
δ_p, δ_n	cm^{-3}	Carrier density
μ_p, μ_n	cm^{2}V^{-1}s^{-1}	Carrier mobility
E	V/cm	External electric field
g'	cm^{-3}s^{-1}	Generation rate
τ_{p0}	µs	Carrier lifetime
$\Delta n, \Delta p$	cm^{-3}	Photongenerated excess carrier density
J_{re}	fA/cm^2	Recombination rate as current density
τ_{eff}	µs	Effective minority carrier lifetime
J_{ph}	fA/cm^2	Photogeneration rate as current density
σ_L	S	Wafer conductance
V_i	kV	Inception voltage of the point electrode
d	cm	Distance from the sharp edge of the electrode to the plane
j(0)	mA/cm^2	planar current distribution directly under the point electrode
j(r)	mA/cm^2	planar current distribution directly at a random point
R	%	Ununiform rate
v	1	Charging speed difference
V_s	V	Surface voltage

List of Acronyms

WBGU	German Advisory Council on Global Change
PERC	Passivated Emitter Rear Cell
c-Si	Crystalline Silicon
SRV	Surface Recombination Velocity
PECVD	Plasma Enhanced Chemical Vapor Deposition
CP	Charge Pumping
CCS	Corona Charging System
ALD	Atomic Layer Deposition
DST	Delft Spectral Technologies
QSSPC	Quasi-Steady-State Photoconductance
µPCD	Microwave Photoconductance Decay
QSS-µPCD	Quasi-Steady-State Microwave Photoconductance Decay
SPV	Surface Photovoltage
CDI	Carrier Density Imaging
QSSV$_{oc}$	Quasi-steady-state Open-Circuit Voltage
PLD	Photoluminescence Decay
LPCVD	Low Pressure Chemical Vapor Deposition
Poly-Si	Polycrystalline Silicon

1 Introduction

1.1 Future Energy System

The energy crisis has been a serious problem for human beings since a few decades. As the pillar of the current energy system, the fossil fuels storage is running to empty; in the meantime, peoples' energy consumption is increasing. The need for a new kind of energy source is urgent. On the other hand, the CO_2 generated by the combustion of fossil fuels causes global warming, it may damage the environment irreversibly. So, renewable energy has become an important issue all over the world. As it is collected from renewable resources, which are naturally replenished on a human timescale. These renewable sources should also produce less side effect to the environment.
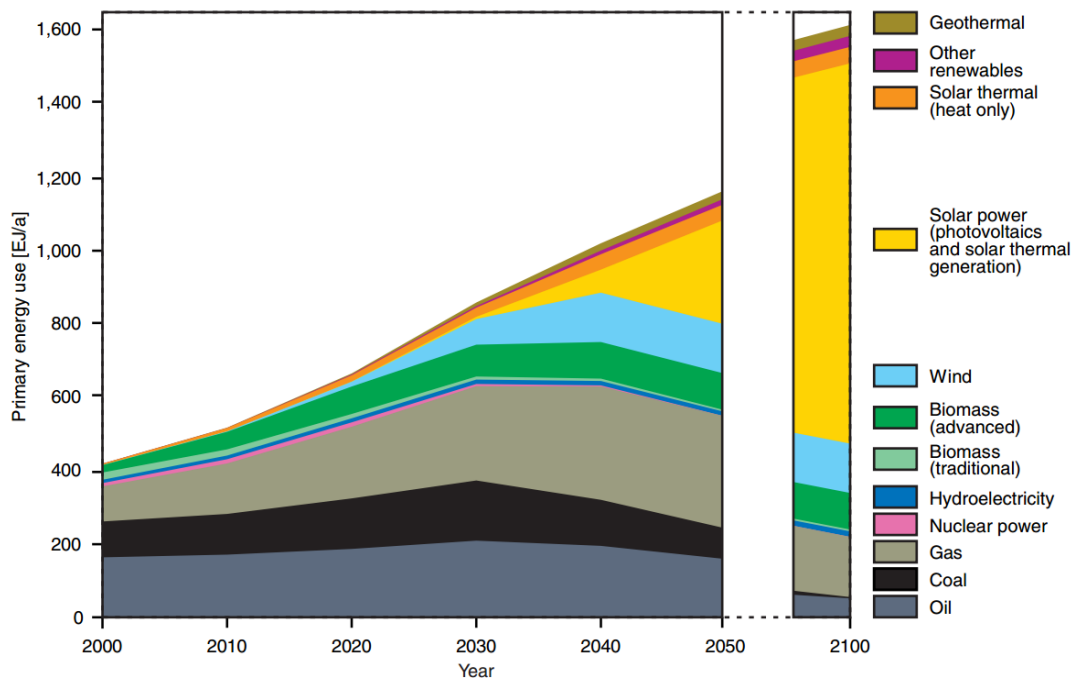
Figure 1-1 Transforming the global energy mix: The exemplary path until 2050/2100[1]

According to the German Advisory Council on Global Change (WBGU), the energy consumption will switch from nowadays fossil fuels to renewable energy. Among all the different kinds of renewable energy, the solar power is in the dominating position. Solar PV is the fastest growing energy technology in the world and reached a level of 76.6 GW of new capacity added annually in 2016. Financial renewable energy experts expect the total global installed PV capacity to exceed 400 GW in 2018, 500 GW in 2019, 600 GW in 2020 and 700 GW in 2021 [2].

1.2 Crystalline silicon photovoltaics

The photovoltaic effect was first discovered by Becquerel in 1839, demonstrating that electrons could interact with electromagnetic radiation [3]. After this milestone discovery, in 1954 crystalline silicon (c-Si) solar cells were invented by Bell Laboratories [4], this made the photovoltaics move out of the theoretical level into applications. From then, the efficiency increased from Bell Laboratories' 6% to 26.6% which is achieved by Kaneka this year [5].
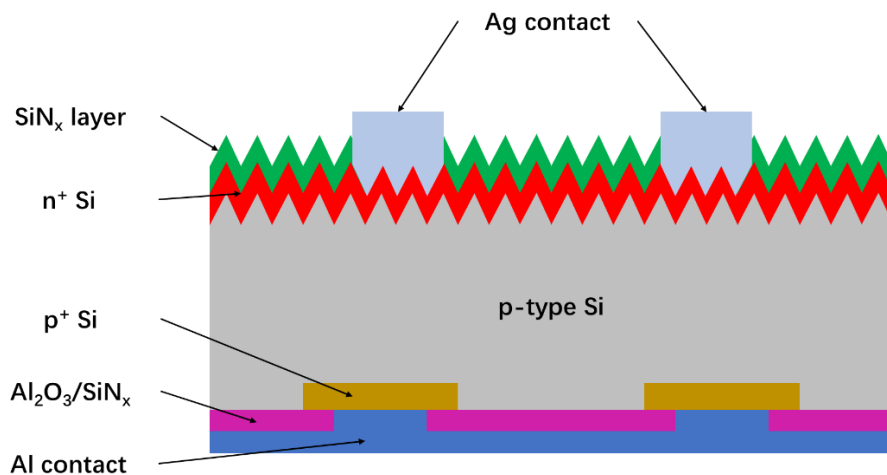
Figure 1-2 schematic of the Passivated Emitter Rear Cell (PERC) c-Si solar cell

The schematic of the Passivated Emitter Rear Cell (PERC) c-Si solar cell concept is shown above. When the sun illuminates on the solar cell, parts of the light will absorb by the solar cell and photons will reach the p-type c-Si bulk. A portion of photons is not able to generate electron-hole pairs as the energy of the photon is low, which is not able to activate the electrons to go across the bandgap of the Silicon (around 1.1 eV). The other parts of the photons with higher energy could generate the electron-hole pairs and separate them to the edge of the bandgap, excess energy of the photons is lost as heat. The electrons recombine with the holes via the external circuit to generate the current.

However, due to the losses, the efficiency could not be extremely high, as mentioned, the c-Si solar cell world record efficiency is 26.6% by Kaneka. The losses come from two main parts, optical losses and electrical losses. For optical losses, the major losses originate from the spectral mismatch, as the low-energy photons could not generate electron-hole pairs, and the high-energy photons could only transform part of the energy into electricity due to

thermalization. Besides the spectral mismatch, there are other losses from reflection, shading, not-complete absorption, etc.

The other main loss is electrical losses, most of the electrical losses comes from recombination. There are two main types of recombination, bulk recombination and surface recombination. Compared these two mechanisms, surface recombination is more important in c-Si solar cell. At the contact surface of two different layers, the defect density is higher than the bulk, because of the interruption to the periodicity of the crystal lattice, which causes dangling bonds at the semiconductor surface. These defects will create some trap states, which stops the electrons to go through the external circuit, and recombine them at the interface. A parameter called the surface recombination velocity (SRV), in units of cm/s, is used to specify the recombination at a surface. If there is no recombination, the SRV is zero; if a surface has infinitely fast recombination, the movement of carriers towards this surface is limited by the maximum velocity they can attain, and for most semiconductors is on the order of 10^7 cm/s.

1.3   Surface Passivation

Applying the suitable material to passivate the surface is one of the most controllable and feasible ways to increase the efficiency. There are two principles for surface passivation. One is chemical passivation, the suitable combination of two different material will reduce the density of interface traps D_{it} on the contact surface. Chemical passivation can be obtained by depositing a thin film on the silicon surface, which binds to the Si dangling bonds. For example, the Si/SiO_2 is well-known for its excellent surface passivation properties. A paper by Fossum and Burgess in 1978 [6] represented a turning point in silicon solar cell technology, showing that a very thin (5 nm) SiO_2 layer thermally grown on a boron diffusion c-Si bulk led to a 30 mV increase in the open-circuit voltage of p+/n/n+ solar cells.

The other principle is the field-effect passivation. As for some materials, there are a certain amount of fixed charge density Q_f inside the material, and these charges will induce a gathering of an opposite polarity of charges gathering on the side of the surface. This clot of the induced charges will create an internal field which repels the minority carrier to float near the surface. It works as a shield to prevent the concentration of the minority carrier near the c-Si surface. However, as the fixed charge has different polarity, a certain polarity could only be used for passivating one kind of doping silicon. For example, as in the PERC solar cell shown in Figure 1-2, for heavily n-type doped surfaces (n+ Si), holes are the minority carriers. The field-effect passivation scheme for such surface therefore ideally has a positive Q_f to reduce the holes concentration.
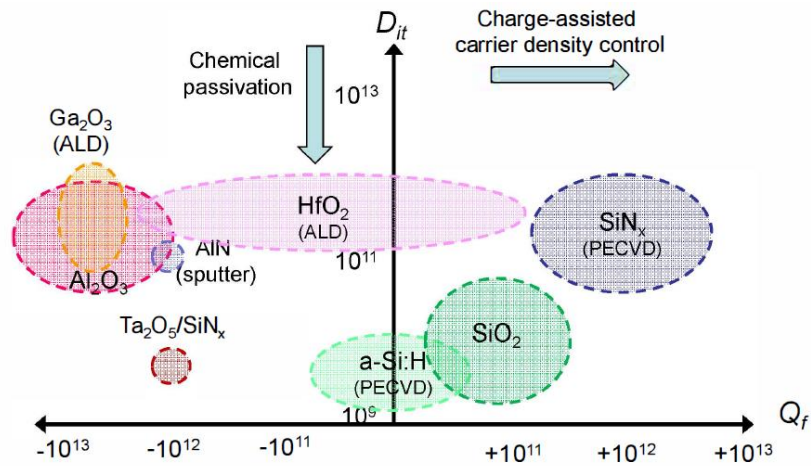
Figure 1-3 Summary of passivating coatings on silicon in terms of fixed charge Q_f and density of interface traps D_{it} [7]

According to Cuevas et al. [7], the amount of the fixed charge Q_f and the density of interface traps D_{it} are shown Figure 1-3. A large amount of the negative fixed charge density is present in Atomic Layer Deposition (ALD) Al_2O_3, and the same scale of positive fixed charge density is shown in Plasma Enhanced Chemical Vapor Deposition (PECVD) SiN_x. These two materials are suitable of p-type and n-type respectively. Also by making a stack of these two materials, the fixed charge density could be manipulated both in amount and polarity. In Figure 1-2, for the PERC solar cell, SiN_x is used for the n+ c-Si passivation, and the SiN_x/Al_2O_3 stack is used for p+ c-Si passivation.

For a specific material, the density of interface traps D_{it} and the amount of the fixed charge Q_f could be used to describe the two different passivation capabilities. For D_{it}, there are many methods to measure it, most of based on MOS capacitors. Besides, Charge Pumping (CP) has been a direct and reliable method to determine gate oxide interface trap density, which can be considered as a direct measure of the interface quality [8]. For Q_f, the most doable method is corona charging testing, which will give an entirely accurate result of the fixed charge density, this approach will be further explored in this thesis.

1.4 Thesis Objective and Structure

1.4.1 Thesis Objective

The work presented in this thesis can be divided into three parts.

The first part of the work is improving the current existing Corona Charging System (CCS) developed by Delft Spectral Technologies (DST), such as increasing the uniformity of the corona charges distribution, adding new functions to the corona charging system, etc.

The second part is using the improved DST corona charging system to test some different materials. Determine the Q_f value for different passivating layers, such as ALD Al_2O_3, PECVD

SiN$_x$, LPCVD poly-Si, etc. Access the suitability of various materials in passivating contacts for c-Si solar cells.

The third part is studying on the decay properties of the corona charges on different materials, and this could be used further for developing the standard test.

1.4.2 Thesis Structure

This thesis will be divided into six chapters, Chapter 1 is the general introduction; Chapter 2 will introduce the principles and settings of the currently existing corona charging system, for example, the corona charger, Kelvin probe and lifetime measurement. Next, in Chapter 3, the improvement of the corona charging system will be illustrated, mainly on increasing the distribution uniformity. Chapter 4 will focus on the experiment, some testing results will be reported, according to the result, the material suitability for corona charging system will be discussed. Chapter 5 shows and discusses the decay properties of the different corona charges in various passivation layers. The last chapter of the thesis will present the conclusion and some recommendations for further studying.

2 Corona Charging System Introduction

2.1 Corona Charging Principle and Setup

The setup for the corona charging is shown in Figure 2-1, the testing sample is placed on a grounded metal plate. Suspended over is the Tungsten needle, a -20kV to +20kV voltage is applied to the needle by the needle power supply V_N.
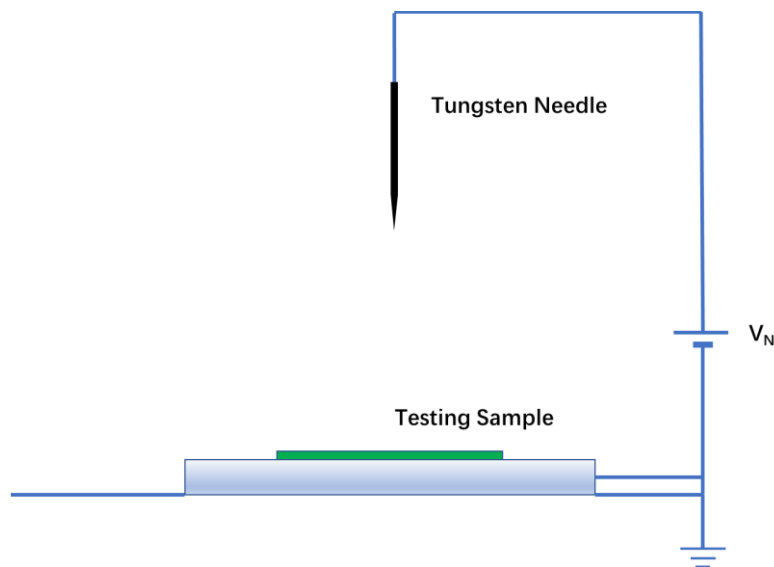
Figure 2-1 Schematic of the corona charging setup, the testing sample is placed on the holder, with a Tungsten needle hanging above it

As a voltage is applied to the Tungsten needle, if the voltage is higher than the corona inception voltage, the sharp edge ionizes the air and generates corona. The corona inception voltage of the sharp edge depends on the radius of the sharp edge and polarity of the voltage. As the air is ionized, the charges with certain polarity come out. Ninety percent of the negative charges consist of CO_3^- ions, whereas for positive charging the main part of the charges consists of hydrated H^+ ions and, additionally, of NO^+ and $NO2^+$ ions for high humidity [9]. The charges follow the electric field between the Tungsten needle and the metal plate then dropping on the sample. As the mean free path is very short at atmospheric pressure, ionized

molecules reach the sample with negligible kinetic energy, therefore without severely damaging the sample surface [10].

If the corona charges deposited on the surface and fixed charge inside the sample are in different polarity, the corona charge will neutralize the fixed charge in the testing sample. For example, if the testing sample is ALD Al_2O_3 deposited on the c-Si, the needle voltage V_N should be positive, then the positive corona generates around the Tungsten needle to drop the positive charges on the ALD Al_2O_3. These positive charges counter the negative charge inside the ALD Al_2O_3, to reduce the fixed charge density in the ALD Al_2O_3. The reduction of the fixed charge density will weaken the field-effect passivation provided by the ALD Al_2O_3, so that more charges will flow to the surface, highly recombination will happen at the surface, leading to a decrease in lifetime and an increase in SRV.

The positive charges keep on gathering on the surface, and the SRV will keep on increasing, when the corona charge density Q_c equals to the fixed charge density Q_f, for the net charges density Q_n:

$$Q_n = Q_c + Q_f = 0 \tag{2-1}$$

there is no field-effect passivation any longer, the SRV will meet its peak value. At this moment, the surface recombination only constraints by the chemical passivation between the two layers.

If the charging continues, the Q_n switches to the polarity of Q_c (for the ALD Al_2O_3 layer, it is positive). As Q_c increasing, Q_n follows increasing, the field-effect passivation increasing again and both the recombination and SRV decrease.

However, when the c-Si bulk is highly doped, then the result may be different to the low-doped wafer. From the work done by Dr. Van der Loo [11], the highly doped SRV will also meet an increase but not going down again.
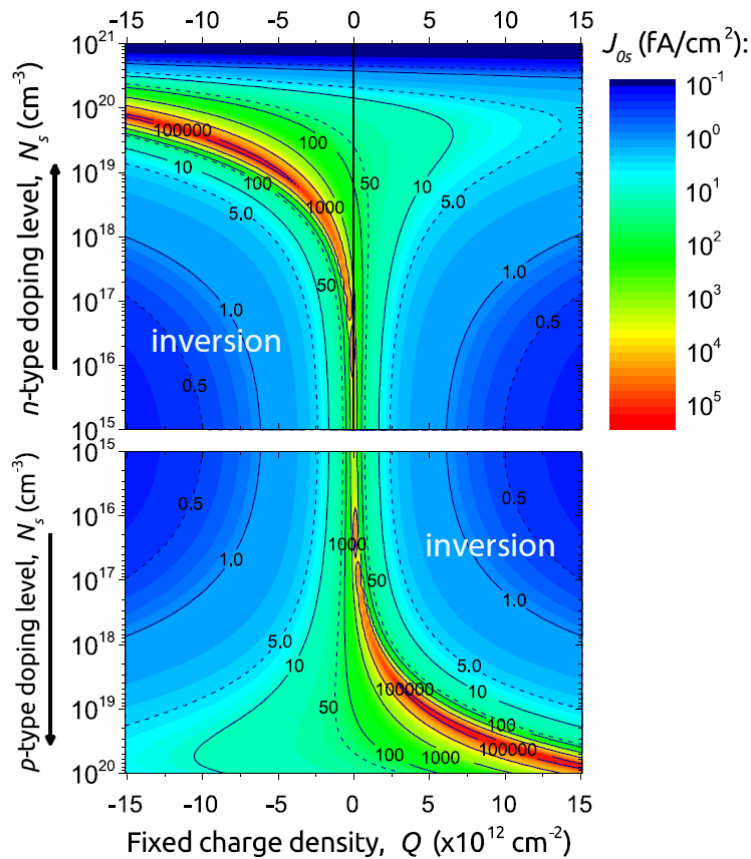
Figure 2-2 The effects of the fixed charge density and the surface doping concentration on the surface saturation current density for a fixed level of chemical passivation. [11]

This phenomenon could be explained by Figure 2-2, for example, a low-doped (10^{15} cm3) p-type silicon passivated by an ALD Al_2O_3 with negative fixed charges (-5*10^{12} cm-2). The starting point will appear on the left top or the graph above. With positive corona charging, it will go horizontally to the right top part, the inversion area. This move leads to an increase then decrease in the surface saturation current density (J_{0s}), which has a positive correlation with the SRV.

However, when it is a highly doped (10^{20} cm3) p-type c-Si wafer, during the corona charging, the J_{0s} will keep on increasing, so the surface recombination current keeps on increasing, and SRV also keeps growing, the turning point could not be seen.

Besides, the corona charging could not be applied to all kinds of materials, as the charges should stay on the sample for a period, if the material is conductive, then the charges will directly go through the sample to the plate which is grounded. In this situation, the material is 'leaky', corona charging is not the suitable method for testing the Q_f value.

Following the features as discussed above, the Q_f value of the material could be tested by using corona charging, if the following four conditions are met:

- The testing material is not leaky.
- The bulk is a low-doped wafer.
- A testing device for the Q_c value
- A machine to track the changing of SRV

The first two conditions are easy to be fulfilled as the testing sample is controllable. For the third one, Kelvin probe is introduced to test how much charge density are deposited on the sample. For the fourth condition, a carrier lifetime time tester would test the real-time lifetime, which will indicate the SRV.

2.2 Kelvin Probe Principle and Setup

The surface charge density on the wafer is measured by Kelvin probe. This technique of capacitive probe measurements is based on the experimental approach of Lord Kelvin [12]. As shown in Figure 2-3, the probe vibrates perpendicular to the test surface, the current flow towards or from the probe depends on the amplitude and the frequency. This current is given according to Equation 2-2:

$$I = \frac{dQ}{dt} = -U * \frac{\varepsilon_r \varepsilon_0 A}{f(\omega, d_0, z)} \tag{2-2}$$

Where U is the voltage between the probe and the sample

ε_r is the relative electric permittivity of the medium between the probe and the sample

ε_0 is the electric permittivity of vacuum ($8.85*10^{-12}$ F/m)

A is the surface area of the probe

z is the vibrating amplitude

d_0 is the distance between the probe and the sample

ω is the vibrating frequency

Here a null method is applied to determine the surface potential. To make the current zero, the probe voltage which is also called compensation voltage to be set to the same value as the surface voltage, which makes the voltage U in Equation 2-2 equals to zero. In other words, when there is no current flow towards or from the probe, the voltage of the probe is the same as the voltage of the sample.
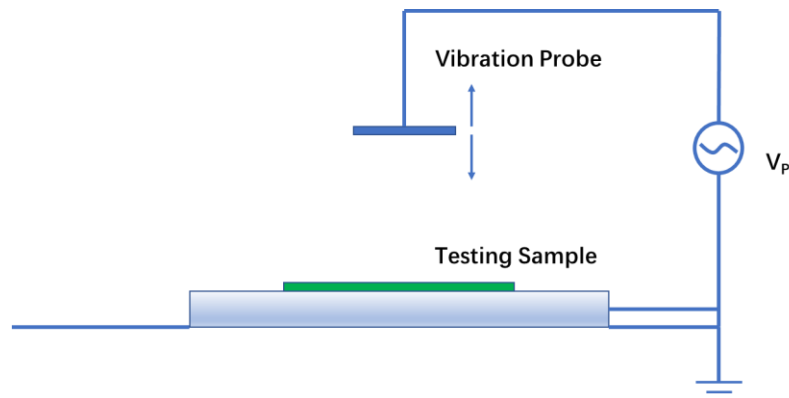
Figure 2-3 Schematic of the Kelvin probe, the testing sample is placed on the holder, a vibration probe vibrating above the sample to test the surface voltage

Trek 325 electrostatic voltmeter is applied for testing the surface potential based on the Kelvin probe principle. As the surface potential of the sample is the same as the voltage on probe which is shown on the screen, according to the equation of the capacitance, the corona charging density Q_c could be calculated by

$$Q_c = \frac{C_s * V_p}{A} = \frac{\varepsilon_s \varepsilon_0 V_p}{d_s}$$

(2-3)

Where C_s is the capacitance of the sample

V_p is the voltage of the Kelvin probe

ε_s is the relative electric permittivity of the sample material

d_s is the thickness of the sample

2.3 Carrier Lifetime Measurement Introduction

For carrier lifetime measurement, the basic principle is the continuity equation [11], which is shown in Equation 2-4 (assuming for an n-type material):

$$D_P \frac{\partial^2(\delta p)}{\partial x^2} - \mu_P E \frac{\partial(\delta p)}{\partial x} + g' - \frac{\delta p}{\tau_{p0}} = \frac{\partial(\delta p)}{\partial t}$$

(2-4)

Where D_p is diffusion coefficient

δ_p is carrier density

μ_p is carrier mobility

E is external electric field

g' is generation rate

τ_{p0} is carrier lifetime

For no external electric field applied and uniformly distributed sample, based on the continuity equation, there are three different modes for testing, which is shown in Table 2-1[13].

It could be easily seen from Table 2-1 that, comparing to the generalized mode, steady-state mode and PCD mode have simpler formulas, which means these modes are easier to achieve. Besides the carrier density, for PCD mode, only the decay speed is required, and for steady-state mode, only the generation rate is required, which will simplify the calculation. From each mode, a unique lifetime testing method is found: Quasi-Steady-State Photoconductance (QSSPC) is based on the steady-state mode; the Microwave Photoconductance Decay (μPCD) is based on PCD mode. Recently, a new method called Quasi-Steady-state Microwave Photoconductance Decay (QSS-μPCD) is a combination of the two approaches above.

Table 2-1 Three different statuses for carrier lifetime measurement

Generalized Mode	$\tau_{p0} = \dfrac{\delta p}{g' - d(\delta p)/dt}$
Transient Photoconductance Decay (PCD) Mode	$\tau_{p0} = \dfrac{\delta p}{- d(\delta p)/dt}$
Steady-State Mode	$\tau_{p0} = \dfrac{\delta p}{g'}$

2.3.1 Quasi-Steady-State Photoconductance (QSSPC)

Quasi-Steady-State (QSS) is a convenient implementation of the steady-state. Achieved by using a pulse of light that varies very slowly compared to the effective lifetime of the wafer (at least ten times slower than the carrier lifetime) [14]. Considering a p-type wafer, under Quasi-Steady-State illumination, the increase in water conductance:

$$\sigma_L = q(\Delta n \mu_n + \Delta p \mu_p)W = q\Delta n(\mu_n + \mu_p)d_s \tag{2-5}$$

Where $\Delta n = \Delta p$ is photongenerated excess carrier density

μ_p, μ_n is the carrier mobility

d_s is the width of the wafer

Photogeneration rate as current density:

$$J_{ph} = J_{re} = \frac{\Delta n q W}{\tau_{eff}} \tag{2-6}$$

Where J_{re} is the recombination rate as current density

τ_{eff} is the effective minority carrier lifetime

Combining Equation 2-5 and 2-6, eliminate the minority carrier surface density, the effective minority carrier lifetime equals to:

$$\tau_{eff} = \frac{\sigma_L}{J_{ph}(\mu_n + \mu_p)} \tag{2-7}$$

Here three parameters are required for calculating the effective carrier lifetime:

Firstly, Carrier Mobility $\mu_n + \mu_p$, it depends on doping type, concentration and excess carrier density. Calculating by software iterative procedure with existing model spreadsheets [15].

Secondly, Photogeneration Current Density J_{ph} is indicated by optical constant (The optical constant equals to 1 is equivalent to a photogenerated current at 38 mA/cm² at 1 sun). This constant could be estimated by PC1D simulations or measurements of the reflectance and transmittance.

Thirdly, wafer conductance σ_L measured though RF bridge circuit inductively coupled to the sample, which is shown in Figure 2-4.
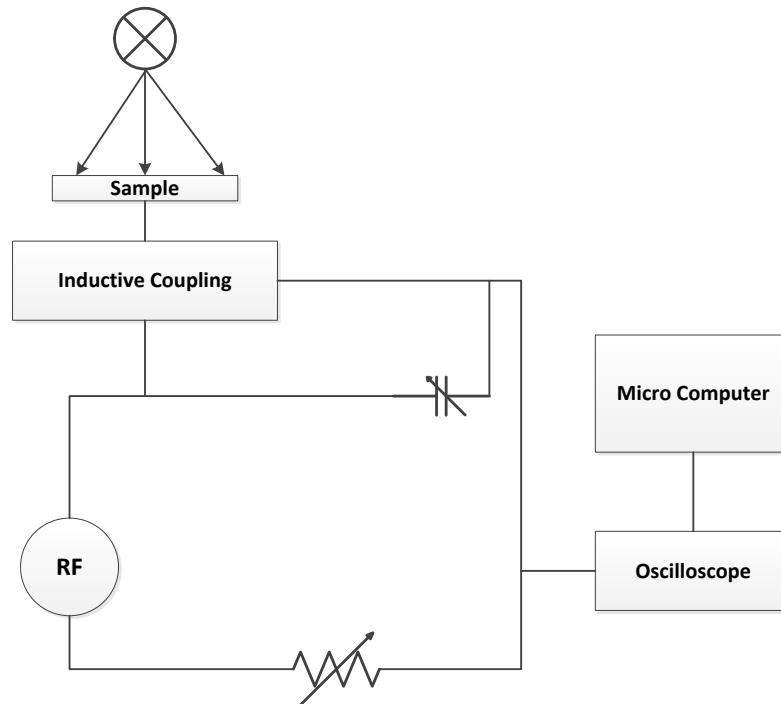
Figure 2-4 RF bridge circuit for measuring wafer conductance, the change in the circuit caused by the illumination on the sample, it could be detected by the microcomputer and calculate the wafer conductance σ_L

2.3.2 **Microwave Photoconductance Decay (µPCD)**

The schematic of the µPCD measuring process is shown in Figure 2-5. Here, periodic laser pulses excite the material generating free charge carriers, which is monitored by the microwave generator. The free charge carriers recombine at recombination centers. The antenna received the reflected microwave power as a function of time. Since the microwave reflection depends on the sample conductivity, the conductivity transient can be measured and evaluated. The transient curve signal is detected by the detector, then sending to the scope. The decay time constant, which is equals to the carrier lifetime is determined directly from exponential fitting of the measured decay curve.
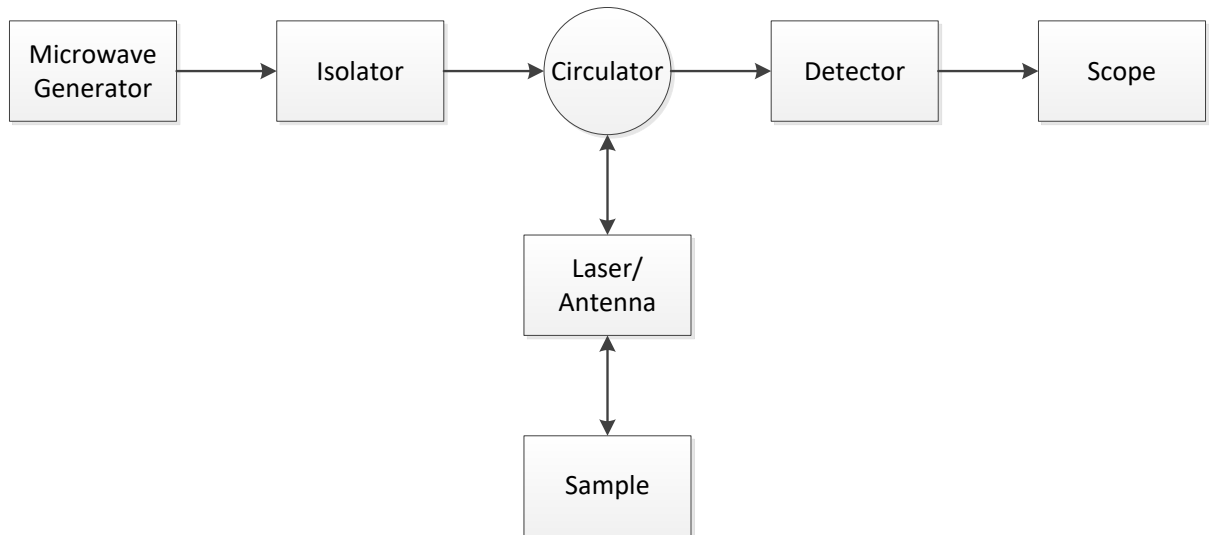
Figure 2-5 Schematic of the µPCD lifetime measuring process, a light pulse is generated by the microwave generator and illuminate and the sample, the reflection wave is detected by the detector and shown on the scope, the decay time constant is equal to the carrier lifetime

2.3.3 **Quasi-Steady-state Microwave Photoconductance Decay (QSS-µPCD)**

According to Wilson et al. [16], a new method is developed for lifetime measurement, and the setup is shown in Figure 2-6.
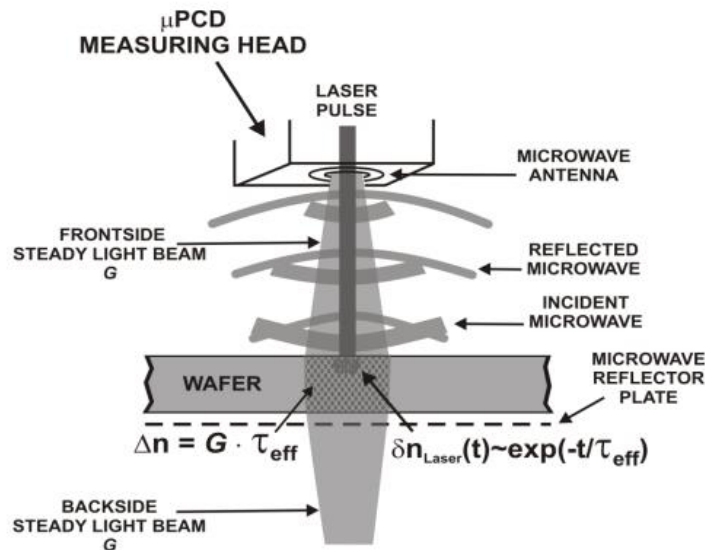
Figure 2-6 Setup for QSS-µPCD lifetime measurement, two light beams illuminate on the sample to create and quasi-steady-state, with a laser pulse to generate the decay, the carrier lifetime is detected with the same method as µPCD [16]

Two steady-state light beams with precalibrated steady-state illumination intensities up to 2 suns are illuminated on the top side and back side, which are used for scanning the generation rate G. The third beam is a short duration (0.2µs) laser pulse with a 905nm wavelength. This pulse generates excess carriers, $\delta n_{laser}(t)$. The first two light beams make sure the wafer is in quasi-steady-state, and the third laser pulse works as same as the traditional µPCD method (also the same measurement system is used here). The laser power is relatively small

comparing to the light beam, which will make the wafer in quasi-steady-state with small perturbation. μPCD methods are used to extract the time constant which equals to the effective carrier lifetime. As the generation rate was known by setting, the minority carrier density could also be calculated.

2.3.4 **Other Methods**

Besides these three methods, other methods could also be adopted to test the carrier lifetime.

- Surface Photovoltage (SPV): Keep the photovoltage constant, changing the incident light wavelength to measure the diffusion length, and then calculate the carrier lifetime.
- Carrier Density Imaging (CDI): Taking two pictures under illumination and darkness, comparing two pictures to find the carrier generation rate, and then calculate the carrier lifetime.
- Quasi-steady-state Open-circuit Voltage (QSSV$_{oc}$): Calculate the open-circuit voltage instead of the conductance to measure the carrier lifetime.
- Photoluminescence Decay (PLD): Used in low carrier lifetime measurement.

Among all the methods mentioned above, as QSS-μPCD is the combination of the other two methods, it absorbs the advantages of each method, and it offers the best accuracy. However, QSSPC and μPCD are more mature in business level, and other methods are used in some special situations or in labs [17]. Comparing these two methods, the QSSPC has a simple calibration that is valid for a broad range of samples, but it required mobility and photogeneration current calculation and some other measurements. μPCD has a high-resolution mapping capability. However, as the laser beam light pulse has a lower limited, when the carrier lifetime is relatively small, this method will lack accuracy; besides, as the laser only covers small piece of sample area, when the carriers on the sample are not uniformly distributed, the result may be disturbed [13, 17]. For the new QSS-μPCD method, the result is comparable towards the QSSPC method [16], but as it is using the laser, the dependence on wafer uniformity still cannot be avoided.

2.4 DST Corona Charging System

2.4.1 **Charging Process of DST Corona Charging System**

Combined all the mentioned parts together, a newly developed Corona Charging System is designed by Delft Spectral Technologies (DST), which is shown in Figure 2-7.
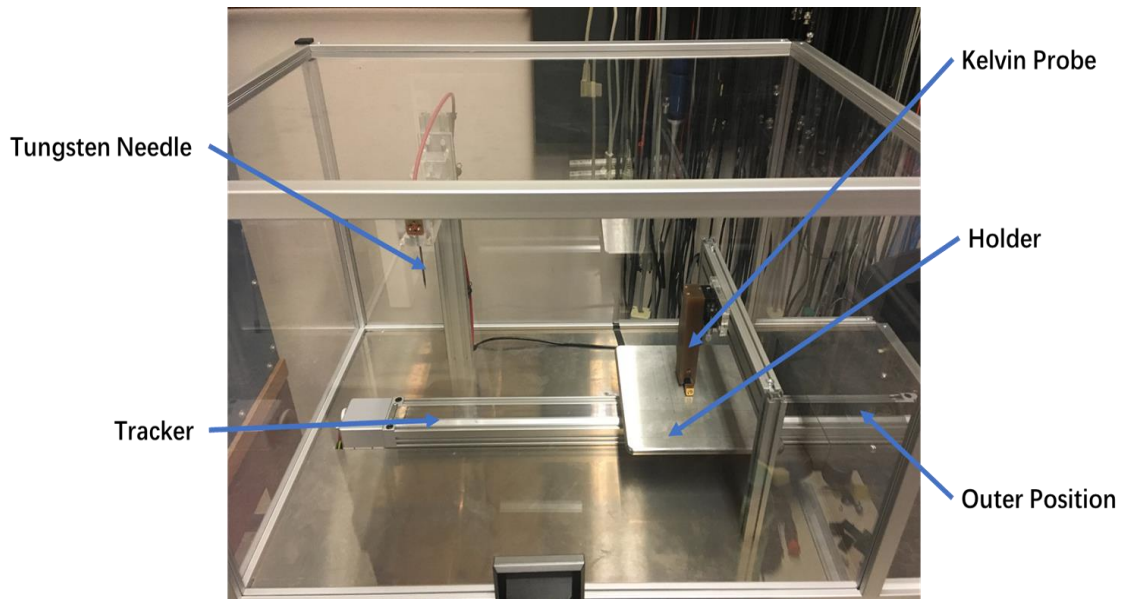
Figure 2-7 DST Corona Charging System, the holder could move on the track, it has three main stops: under corona charger, under Kelvin probe, at outer position, each stop was designed for special functions

From Figure 2-7, a full run of the corona charging testing will be:

1. Place the testing sample on the holder, when the system starts, the holder will be located at the outer position.
2. Move the sample under the Kelvin probe through the track, the starting surface voltage value of the sample will be determined. Then, move the holder back to the outer position, flip the sample over, then testing the starting surface voltage on the other side.
3. Set the corona charging voltage and the corona charging time, then move the holder under the corona charger to start charging. As soon as the charging finished, move the holder back to the outer position, and then flip the sample over again. After flipping, directly move the holder under the corona charger to charge the starting top side of the sample.
4. After charging both sides of the sample, move the holder back to the outer position, pick up the sample to the lifetime measurement machine, measure the carrier lifetime.
5. Repeat the entire process until the peak has been seen, several more runs need to be taken to draw the whole curve.

For current corona charging system, the outer position is empty, in the future, a carrier lifetime measurement device will be integrated into the system in that place to make the entire system run automatically.

2.4.2 Unique Features of DST Corona Charging System

Compared to the traditional corona charging system, the DST corona charging system has some unique features need to be mentioned:

- For the corona charging part, the needle directly points to the centre of the holder, the needle height (from the sharp edge of the needle to the holder) is 14.5cm, this height is adjustable. The voltage on the needle could be adjusted from -20kV to +20kV.
- The control unit of the Kelvin probe from the Trek 325 electrostatic voltmeter. As the holder moves automatically, the Kelvin placed 1.2 mm above the holder, to prevent the sample scratching the Kelvin probe.
- For the current situation, the Sinton WCT-120 with QSSPC method is applied for carrier lifetime testing, all the testing results are carried out with this lifetime tester. For the future system update, other methods may be applied.
- The entire system is supplied by a 24V power supply, and the entire system will be shut down by pressing the power button, at the back of the system box.
- For safety reasons, the Kelvin probe and the corona charger are covered by a plastic box, as the working voltage is too high.

3 Improvement of the Charge Uniformity

3.1 Warburg's Law

For the corona charging system, one important index is the charging uniformity. For a certain corona generated from the needle to drop on a flat surface, the corona charge distribution follows the Warburg's Law, which reveals the point to plane charge distribution in air, the schematic of the point to plane corona is shown in Figure 3-1.
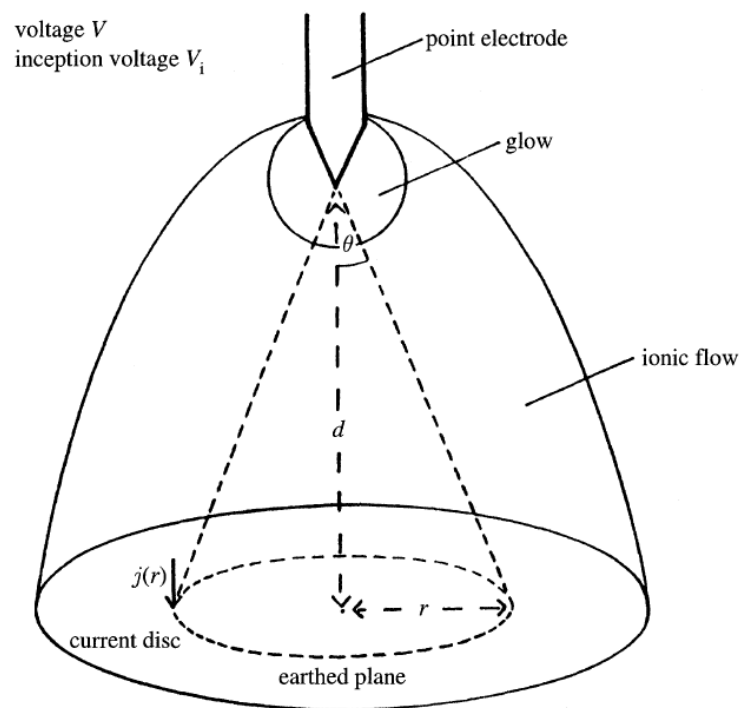
Figure 3-1 schematic of the point to plane corona, the relative parameters are shown in figure [18]

For the value of planar current distribution of a certain point with a distance r from the center (center is the point on the plane which directly under the point electrode), j(r) is shown in Equation 3-1

$$j(r) = j(0)cos^m(\theta) \tag{3-1}$$

17

Where j(0) is the value of planar current distribution directly under the point electrode

   m is a constant

For constant m, according to the classical experiments of Warburg [19], he found that the best representation of experiments was obtained for m = 4.65 for a negative corona, and for m = 4.82 for a positive corona. For general use, the m value is set to 5 for both positive corona and negative corona.

For the value of planar current distribution directly under the point electrode, j(0) could be derived from Equation 3-2

$$j(0) = k\frac{V_N(V_N - V_i)}{d^3} \qquad (3\text{-}2)$$

Where k is a constant

   V_N is the voltage on the point electrode

   V_i is the inception voltage of the point electrode

   d is the distance from the sharp edge of the electrode to the plane

Here V_i is the inception voltage of the point electrode, only when the voltage on the point electrode V_N is higher than inception voltage, the corona could be generated. In Equation 3-2, V_N-V_i is always positive, the sign of j(0) only depends on the voltage on the point electrode V_N.

As the j(r) indicates the current distribution, it will also show the charge distribution as well, by calculating the j(r) value of each point, the corona charge distribution will be found. For current system calculating, during a single run j(0) will not change, so the angle θ will be the only factor that influences the corona current distribution. However, if adjusting the system, especially changing the distance between the point electrode and the plane, there will be value changes for both j(0) and $\cos^5(\theta)$.

Warburg's Law is known to be valid from small gaps of a few millimeters to large gaps of several meters [20, 21], which contains the setting distance for the DST corona charging system. Besides, when the angle θ is higher than 60 degrees (θ>60°), Warburg Law's is not valid anymore.

3.2   Single Needle System

3.2.1   System setup

The single needle corona charging system is shown in Figure 2-1, the needle height set as 14.5 cm. For testing the uniformity, the sample experienced a certain amount of charging time. Line mapping function is applied to test the uniformity result, as the charge density has the same value with a specific radius from the center, the distribution is symmetric, so testing one line instead of the whole holder could give the same result. Nine random points are picked on

the line to trial the surface voltage, there is randomly 1-2.5cm distance between each point, the total mapping distance is 13cm.

All the tests are carried out with an ALD Al_2O_3 capping layer deposited on the c-Si wafer. For ALD Al_2O_3, the charges on the sample will stay longer than other potential materials, which will be mentioned in Chapter 5.

3.2.2 Uniformity Testing Result

The result is shown in Table 3-1, using the voltage instead of the surface charge density to show the distribution, as uniformity is the only concerned value, the exact surface charge density does not need to be calculated. Here the wafer has been charged for 5 minutes with 10kV corona charging voltage.

Table 3-1 Uniformity testing result for single needle system

Testing Point	1	2	3	4	5	6	7	8	9
Surface Voltage Difference (V)	1.41	1.62	1.86	2.12	2.31	2.02	1.81	1.58	1.34

According to Table 3-1, Figure 3-2 is drawn to compare the experiment result to the theoretical result calculated by the Warburg's Law.
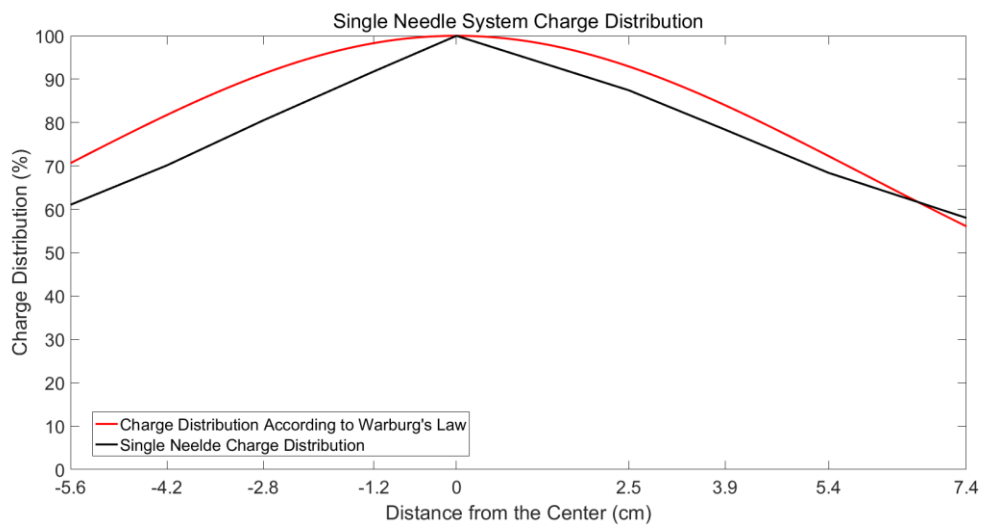
Figure 3-2 Single needle charge distribution, comparing with the distribution curve derived from the Warburg's Law

The black line is the testing result, according to Bonilla, Woodcock, and Wilshaw from Oxford [22], they reported a 4% difference in uniformity with a 3*3 cm² sample, with the needle height 15 cm. However, although the setting needle height is comparable to the Oxford setting, for the 3*3 cm² square, our difference is more than 20%.

Also, comparing to the theoretical result given by Warburg's Law, the testing uniformity is also lower, especially on the left side of the needle, this is due to the grounded box column on

the left side, which may influence the electric field distribution and then influence the charge distribution.

3.3 Multiple Needles System

3.3.1 System Setup

The system setup is the same as the single needle system, and the only difference is that there are multiple needles instead of one single needle. The top view of the system is shown in Figure 3-3, the blue square represents the holders, and the green square represents the testing sample, the black dots represent the needles, for the Figure 3-3 it is a four needles system. As each needle follows the Warburg's Law, if the charges distribution in certain position generated by all the needles superimposing properly, then the total charge distribution will be uniformly distributed.
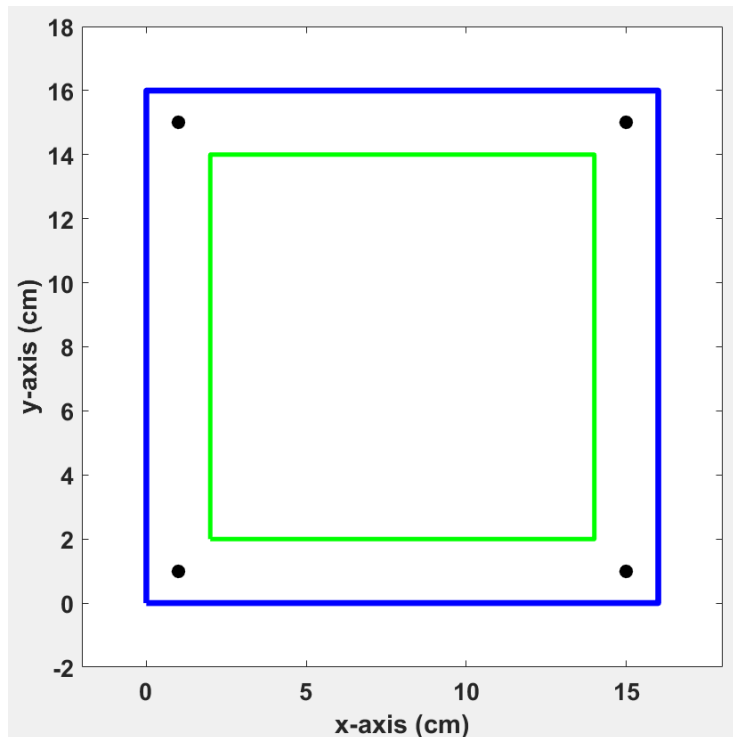
Figure 3-3 Top view of the four needles system, blue square represents the holder, green square represents the sample, black dots represent the needles, the size of the holder and sample indicate by the coordinate

However, as both the number of the needles and the needle positions are unknown, the simulation was taken to optimize all these factors.

20

3.3.2 Simulation of the Multiple Needles System

3.3.2.1 Simulation Method

As the charge distribution follows the Warburg's Law, if one needle's height is fixed, also with a certain voltage, then the j(0) could be calculated; if the position of the needle is also given by the coordinate, for example, in Figure 3-2 four needles are located at (1,1), (1,15), (15,1), (15,15), all the coordinates with the unit of centimeter. For a random point on plane, the angle θ to each needle could also be calculated. As the θ and j(0) are known, the current distribution of a random point j(r) could be calculated by superimposing the charge distribution generated by each needle.

$$j(r) = j_1(r) + j_2(r) + j_3(r) + \cdots\cdots + j_n(r) \tag{3-3}$$

To simulate the charge distribution. One of the needles located at the diagonal of the holder square as the reference needle, which is shown in Figure 3-4. Using the reference needle to represent all the needles' positions, as the reference needle position changes, as other needles are rotational symmetric of the holder center, which positions will also change in the symmetric way. The moving step is set as 1cm inside the holder and 0.5cm outside the holder. The moving range is from (8, 8) the center to (-5, -5) which is limited by the entire system size.

For simplifying the simulation, all the needles are on the same height level. For each needle position, the distance between the needle and the platform is varying from 0cm to 100cm with a step of 0.5cm. For each distance, calculating the charge speed difference and the ununiform rate to draw the curve and find the suitable value.

Here four needles, five needles, six needles, eight needles system are tested to find out the most suitable plan for multiple needles system.
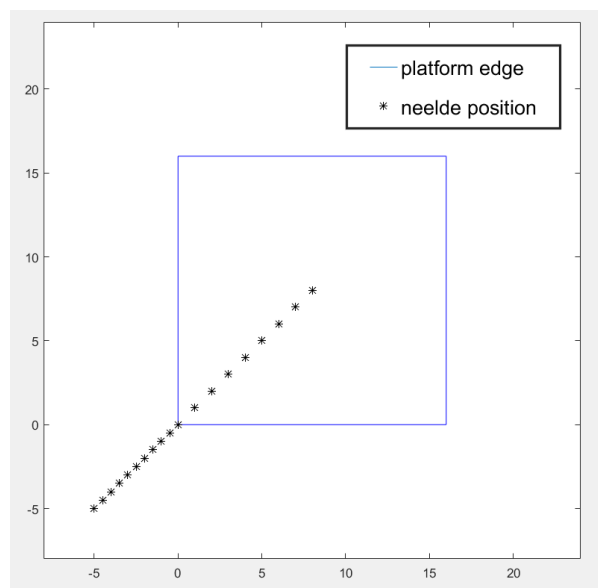
Figure 3-4 Schematic of the reference needle moving track, the blue square represents the holder, the star dots represent the needles

21

As discussed with DST, four indexes are used to evaluate the corona charge distribution:

1. Ununiform Rate: R<5%

$$R = \frac{j(max) - j(min)}{j(max)}$$

(3-4)

2. Charging Speed Difference: v<0.3 (Comparing to the single needle system):
3. Needle Height: d<23cm (defined by the system size)
4. Sample Edge to needle angle θ_{max}<60° (Warburg's Law limited)

3.3.2.2 Four Needles Systems

As mentioned above, for a chosen needle position, the ununiform rate and charging speed curve against the needle height could be drawn, which is shown in Figure 3-5.
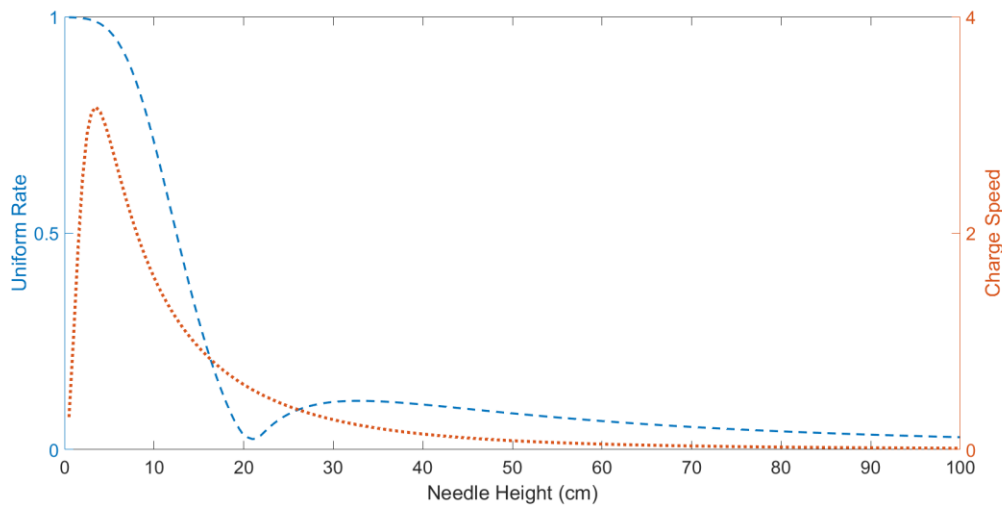
Figure 3-5 Ununiform rate and charging speed curve against the needle height, with reference needle position (-2, -2) (blue: ununiform rate; orange: charging speed)

Figure 3-5 is drawn with the reference needle position located at (-2, -2). For the charging speed, which is indicated by the j(0). There will be a peak in the curve at a certain needle height then drops down, however, at the peak point of the charging speed, the ununiform rate is too high which is not acceptable. So, the needle height could not be decided by the peak point of the charging speed. For the ununiform rate, there is a valley point in the curve during the change of the needle height, which could give the best uniformity of corona charges, at the same time, the charge speed is not very slow, so according to the Figure 3-5, the corresponding x-axis coordinate of the valley point is the optimized needle height for the reference needle at (-2, -2) position.

By choosing the valley point of the ununiform rate curve, the optimized height of each needle position could be found, judging the result by the four indexes to find the best needle position and height pair, the result is shown in Table 3-2.

22

Table 3-2 Simulation result of the four needles system

Coordiante	R(%)	v	d(cm)	OK?
8,8	no lowest point			
7,7	no lowest point			
6,6	no lowest point			
5,5	no lowest point			
4,4	no lowest point			
3,3	43.58	3.36	11	1,4
2,2	23.32	3.03	11	1,4
1,1	11.73	1.95	13	1
0,0	6.13	1.16	16	1
-0.5,-0.5	5.05	0.97	17	1
-1,-1	3.76	0.78	19	ok
-1.5,-1.5	2.92	0.64	20.5	ok
-2,-2	2.42	0.55	21.5	ok
-2.5,-2.5	1.94	0.46	23	ok
-3,-3	1.64	0.4	24	3
-3.5,-3.5	1.37	0.34	25	3
-4,-4	1.15	0.3	26	2,3
-4.5,-4.5	0.98	0.27	27	2,3
-5,-5	0.86	0.24	28	2,3

From Table 3-2, for four needles system, the optimized reference needle position is from (-1, -1) to (-2.5, -2.5), and the corresponding needle height d is given in the table. As from (8, 8) (all in the center) to (4, 4), the ununiform rate will not have a valley point during height changing. For position (2, 2) and (3, 3), the minimum ununiform rate is too high and with the optimized height, besides, at the edge of the platform does not obey the Warburg's Law. For position (1,1), (0,0), (-0.5, -0.5), the lowest ununiform rate is not lower than 5%. For the position from (-3, -3) to (-5, -5), the needle height should be more than 23cm to reach the best uniformity, which exceeds the system setting size, what is more, for positions (-4, -4), (-4.5, -4.5), (-5, -5), these positions charging speed is too slow, which is also not acceptable.

3.3.2.3 Five Needles System

Table 3-3 Simulation result of the five needles system

Coordiante	R(%)	v	d(cm)	OK?
8,8	no lowest point			
7,7	no lowest point			
6,6	no lowest point			
5,5	no lowest point			
4,4	no lowest point			
3,3	no lowest point			
2,2	no lowest point			
1,1	21.74	2.08	14.5	1
0,0	13.19	1.51	16	1
-0.5,-0.5	10.15	1.33	16.5	1
-1,-1	7.83	1.12	17.5	1
-1.5,-1.5	6.05	0.95	18.5	1
-2,-2	4.7	0.81	19.5	ok
-2.5,-2.5	3.7	0.67	21	ok
-3,-3	2.9	0.58	22	ok
-3.5,-3.5	2.38	0.49	23.5	3
-4,-4	1.88	0.43	24.5	3
-4.5,-4.5	1.62	0.37	26	3
-5,-5	1.28	0.33	27	3

As shown in Table 3-3, the green light position range for five needles system is from (-2, -2) to (-3, -3).

3.3.2.4 Six Needles System

Table 3-4 Simulation result of the six needles system

Coordiante	R(%)	v	d(cm)	OK?
8,8	no lowest point			
7,7	no lowest point			
6,6	no lowest point			
5,5	no lowest point			
4,4	no lowest point			
3,3	no lowest point			
2,2	no lowest point			
1,1	18.98	3.05	13	1
0,0	9.96	2.15	14.5	1
-0.5,-0.5	7.31	1.68	16	1
-1,-1	5.41	1.41	17	1
-1.5,-1.5	4.09	1.14	18.5	ok
-2,-2	3.32	0.93	20	ok
-2.5,-2.5	2.5	0.8	21	ok
-3,-3	2.1	0.67	22.5	ok
-3.5,-3.5	1.68	0.59	23.5	3
-4,-4	1.42	0.5	25	3
-4.5,-4.5	1.13	0.45	26	3
-5,-5	1.03	0.38	27.5	3

24

As shown in Table 3-4, the green light position range for six needles system is from (-1.5, -1.5) to (-3, -3).

Table 3-5 Simulation result of the eight needles system

Coordiante	R(%)	v	d(cm)	OK?
8,8	no lowest point			
7,7	no lowest point			
6,6	no lowest point			
5,5	no lowest point			
4,4	no lowest point			
3,3	no lowest point			
2,2	30.83	5.89	11.5	1,4
1,1	15.19	4.7	12	1,4
0,0	7.82	2.87	14.5	1
-0.5,-0.5	5.77	2.25	16	1
-1,-1	4.62	1.79	17.5	ok
-1.5,-1.5	3.6	1.52	18.5	ok
-2,-2	2.79	1.24	20	ok
-2.5,-2.5	2.42	1.07	21	ok
-3,-3	1.81	0.9	22.5	ok
-3.5,-3.5	1.64	0.79	23.5	3
-4,-4	1.26	0.67	25	3
-4.5,-4.5	1.11	0.59	26	3
-5,-5	0.94	0.51	27.5	3

As shown in Table 3-5, the green light position range for eight needles system is from (-1, -1) to (-3, -3).

Compared all the multiple needles system results given above, for all the multiple needles systems, there will be a certain position range which could meet the uniformity requirement. At last, the four needles system is chosen as fewer needles are required, and it is easier to fabricate the four needles charging device.

3.3.3   Uniformity Testing Result

When the needle is located at the optimized position chosen by simulation, after charging, no charges could be found in the center of the wafer. According to Jones [23], when there are multiple corona generators, the generators will influence each other. There will be a strong interaction of the electric field, the tail of the electric field will be cut, which means the corona generators will influence only the small area directly below the needle. When the needles are too far away from the center, the effective area could not cover the center of the wafer, which makes the no charge drops in the center. Besides, from Jaworek & Krupa [24], each needle's inception voltage should also be increased, as there are four needles staying closer.

Understanding the issues above, a new position has been set for the reference needle, which is (2.34, 2.34), located inside the wafer area. The charging time is 5 minutes with the charging

voltage 18kV as the inception voltage of each needle increasing. The result is shown is Table 3-6.

Table 3-6 Uniformity testing result for four needles system

Testing Point	1	2	3	4	5	6	7	8	9
Surface Voltage Difference (V)	0.70	0.72	0.74	0.74	0.55	0.62	0.75	0.73	0.67

The figure of the distribution is shown in Figure 3-6. The charge density is still low in the middle. However, comparing to the simulation optimized position, the result is much better. The entire charge distribution is also better than the single needle system, in spite of the interaction is still a problem to the multiple needles system.
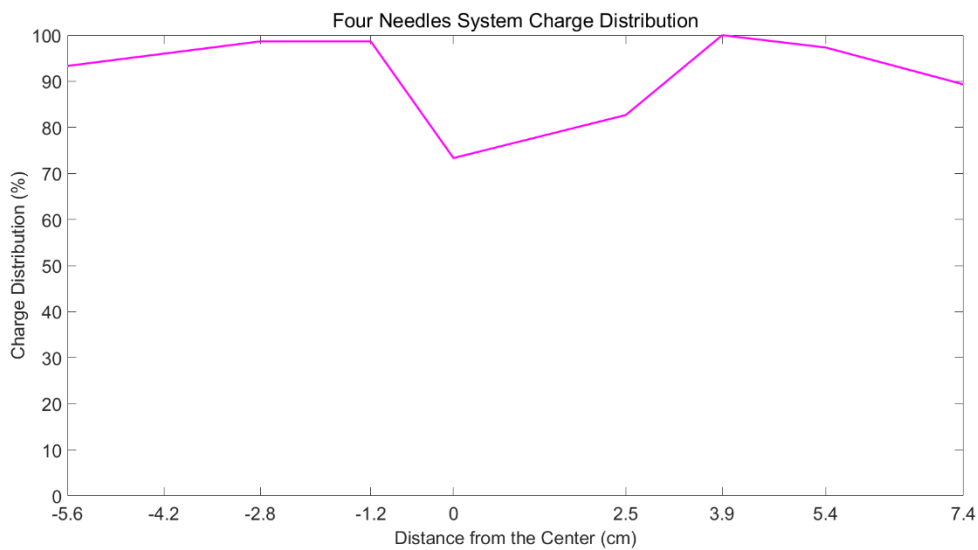
Figure 3-6 Four needles system charge distribution

3.4 Single Needle Mesh System

3.4.1 System Setup

For the single needle mesh system, a metal grid has been inserted between the needle and the platform. By adding the electrify grid, the whole system becomes a corona triode system [25], as shown in Figure 3-7, A metallic point is connected to HV supply V_N to produce corona ions which are driven towards the sample. A conductive grid, biased by a voltage supply, V_G, is inserted into the point-to-sample gap, the grid is 1cm above the sample.

As there is a grid between the needle and the sample, instead of directly heading towards the sample, the charges will firstly deposit on the grid then followed a uniformly distributed electric field towards the sample. As the grid is in a higher position than the sample, according to Warburg's Law, the distribution will be better.

According to M. M. Mandoc et al. the voltage on the grid should be around 10V [26]. However, the voltage does not work for the DST settings, after carefully comparing these two systems, for DST settings, the voltage on the grid should be around 2.5kV to make the system work properly. As the power supply from DST has a lower resistance comparing to resistance of the air between the mesh and the sample, the charges will not drop through air to the sample, but go through the power supply circuit to the ground. In case of that, a very high resistor (2.5GΩ) was connected between the power supply and the mesh to block the charges go through the power supply, even though, the current through the power supply has been measured around 1μA.

Although the current is relatively low, there is high resistance series connected in the system to make the voltage drop on the grid in kV range. For using the 10V power supply, I think the actual voltage on the grid will also be in the same magnitude.
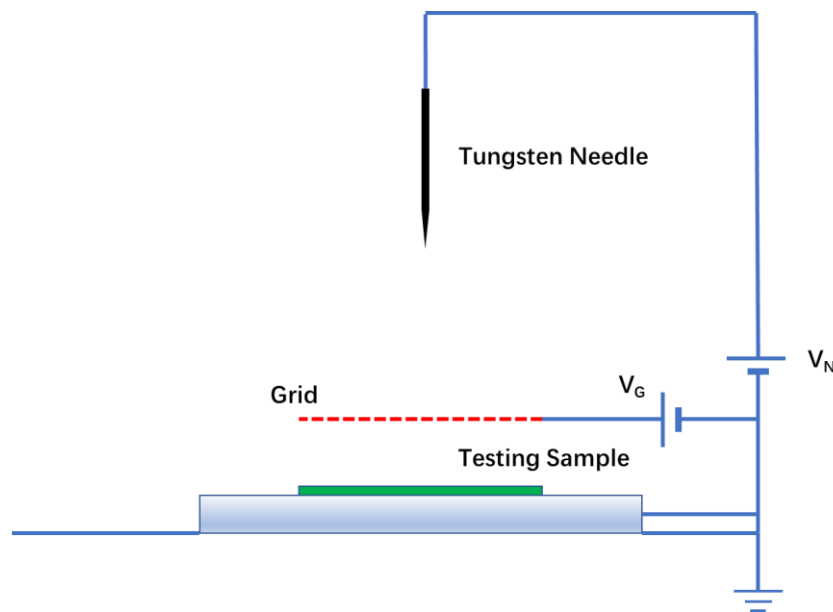
Figure 3-7 Schematic of the Single Needle Mesh System, a grid is added between the testing sample and the Tungsten needle, a suitable grid voltage V_G is applied to the grid

Comparing to the single needle system, the speed of charging will also decrease. As part of the charges will go through the power supply to the ground, which makes the corona charge density drop on the testing sample lower than the same setting without the grid.

To improve the corona triode system, a control loop is introduced [27], when charges deposit on the sample surface, the surface voltage of the sample increases. When the surface voltage equals to the grid voltage, then there is no electric field in between, which will stop the charges dropping down to the sample. The control loop is used to give feedback to the grid power supply V_G to increase the voltage on grid. However, in the fixed charge testing, the surface voltage will not reach that magnitude, so no control loop is required for the corona charging device.

3.4.2 **Uniformity Testing Result**

As the fewer charges will drop on the sample, to drop the nearly same amount of charge, more charging time is required, for the single needle mesh system, 9 minutes charging for testing the uniformity with 10kV corona voltage. The testing result is shown in Table 3-7.

Table 3-7 Uniformity testing result for single needle mesh System

Testing Point	1	2	3	4	5	6	7	8	9
Surface Voltage Difference (V)	0.71	0.91	1.06	1.13	1.22	1.16	1.09	0.99	0.83

The figure of the distribution is shown in Figure 3-8.
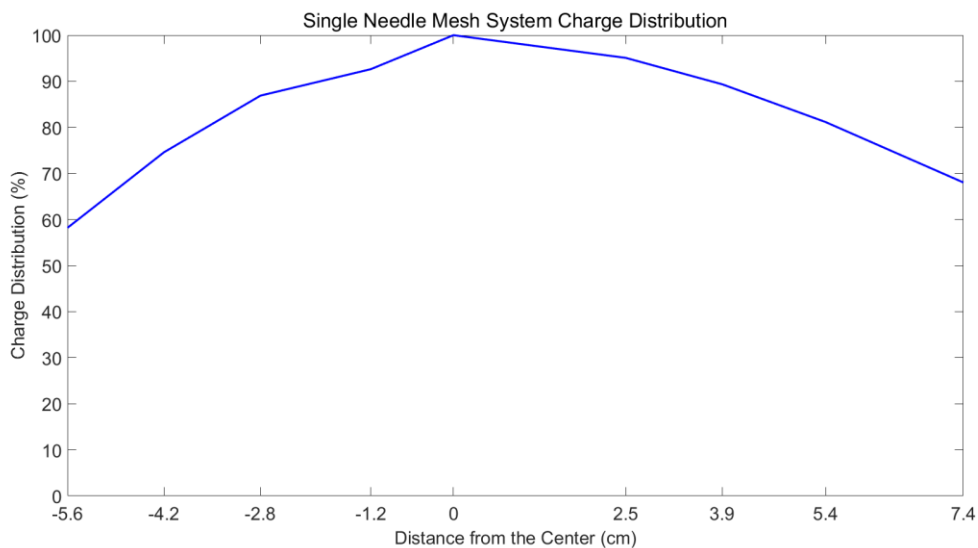
Figure 3-8 Single Needle Mesh System Charge Distribution

From Figure 3-8, compared to the single needle system, the charge uniformity is improved, especially in the 1.5cm to 3cm range, where the charge density is almost close to the charge density in the center. Around 15% difference is shown in 3cm radius. This setting is suitable for a traditional 4-inch wafer, as it covers most parts of the wafer. However, if the wafer radius increases, for example, the 6-inch cutting edge wafer for industrial application, this method is not suitable anymore.

Besides, according to Adam, he had made some improvements like adjusting the distance between the grid and the sample, changing the grid size, etc. [28] However, none of them could reach a uniformly distributed charge over a 6-inch wafer.

3.5 Rotation Charging System

3.5.1 System Setup

Because of the interaction between the needles, the multiple needles system does not work as expected. However, if the interaction could be eliminated, then the system may work on its function. Here the rotation charging system is designed. The system setup is almost the same as the single needle system. However, the needle is no longer point to the center of the holder, but located at the place of the reference needle's position in multiple needles system. There is a rotator under the holder, to make the holder able to rotate.
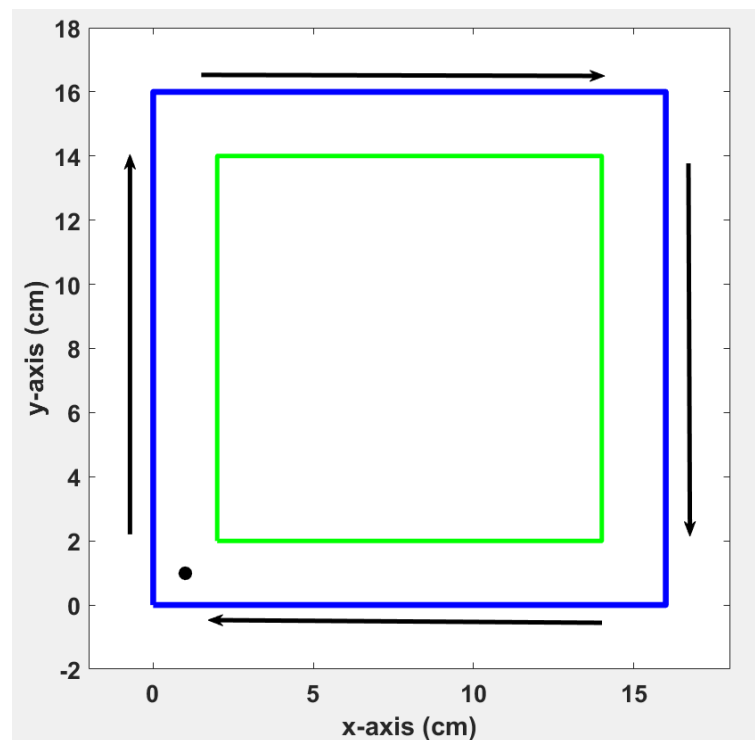
Figure 3-9 Top view of the rotation charging system, blue square represents the holder, green square represents the sample, black dots represent the needles, the size of the holder and sample indicate by the coordinate

The top view of the system is shown in Figure 3-9, after a single charging round, the holder rotates 90 degrees, then charging again for the same amount of time. Changing like this for four times could have the same result as the four needles charging system without the interaction.

The same function could be achieved by rotating the needle, however, as the needle in under high voltage, the rotator needs a reliable insulation which will cost more money.

3.5.2 Uniformity Testing Result

Due to some issues, this system is still under construction. However, this setup could be achieved by changing the needle position by hands. After each charging time, shut down the electricity, then put the needle in another position. The needle positions are located same as

the four needles system, with the charging voltage 10kV. The result of the system is shown in Table 3-8:

Table 3-8 Uniformity testing result for rotation charging System

Testing Point	1	2	3	4	5	6	7	8	9
Surface Voltage Difference (V)	0.49	0.54	0.57	0.52	0.51	0.58	0.54	0.54	0.46

The figure of the distribution is shown in Figure 3-10. Compared to the four needles system, more charges are dropping in the center of the wafer, the whole difference is below 20%, which could not be reached by all the systems above.
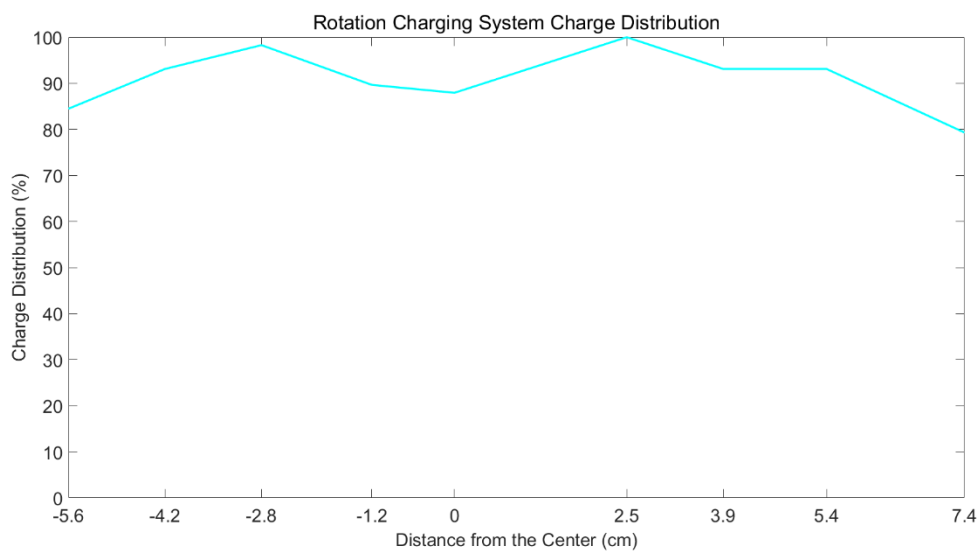
Figure 3-10 Rotation Charing System Charge Distribution

3.6 Comparison of Different Setups

Figure 3-11 comparing all the results from different charging systems.
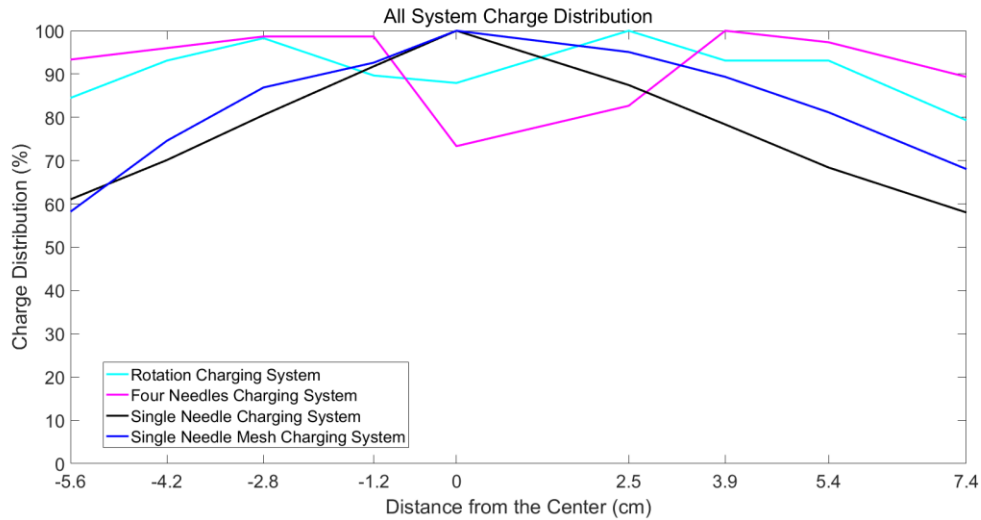
Figure 3-11 All charging System Distribution Comparing (Black: single needle charging system; Pink: four needles charging system; blue: single needle mesh charging system; Cyan: rotation charging system)

From Figure 3-11:

The rotation system is the best solution for making the charge uniformly distributed. It could create a less than 20% difference in the whole mapping line. However, this method is hard to achieve as a new rotor must be added under the holder.

Four needles system is influenced by the interaction between the needles. It also shows a good performance in uniformity, however, as the corona inception voltage increasing, the system must be worked at around 18kV which almost reach the upper limit of the system (20kV).

Single needle mesh system also performs better than traditional single needle system. The system is also easy to achieve, but it will spend more time than the single needle system as part of the charges will go through the voltage supply to the ground.

Single needle system could only generate a small area for uniformly distributed charges with less than 20% difference in 2*2 cm² area. As this area is bigger than the sensor area of the Sinton machine, it means that if the sample is always placed in the same position, and the passivation layer is deposited flatly, the fixed charge density could also be tested out. However, if there are different thickness on one sample, this method will not work any longer.

4 Experimental Result

4.1 Corona Charging on ALD Al_2O_3

The ALD Al_2O_3 is known for large amount of negative fixed charge density, which is good for p+ c-Si surface passivation, for highly doped n+ c-Si bulk, the level of passivation provided by ALD Al_2O_3 is in many cases found to be compromised due to its negative Q_f [29]. However, when the doping is low inside the c-Si bulk, the ALD AL_2O_3 works well for both n-type and p-type. For the whole experiment, the n-type low-doped (10^{15} cm^{-3}) c-Si wafers are used as the bulk material, with different deposition layers on top of it.

As the system is the first automatic corona charging system, the first important issue is testing whether the system is as good as the traditional corona charging system. As the ALD Al_2O_3 is most commonly tested material for the corona charging system, here using it to test whether the system works for the material with a negative Q_f (positive corona charging).

4.1.1 Sample Preparation

22nm Al_2O_3 is deposited on both side of the mirror polished 280 μm c-Si sample by atomic layer deposition, then the ALD Al_2O_3 samples were all annealed in N_2 gas at 400 °C for 10 minutes, which is the standard optimized annealing treatment in terms of the lifetime. The schematic of the sample is shown in Figure 4-1.

Figure 4-1 Schematic of the double side mirror polished sample, 22nm Al_2O_3 was deposited on the low-doped n-type c-Si bulk by ALD process

4.1.2 **Experimental Result**

On all the testing samples, corona charging was carried out on both sides, sequentially, for equal amounts of time. According to Chapter 2, the surface voltage is tested by Kelvin Probe and the carrier lifetime is tested by the Sinton WCT-120 lifetime tester, the original data is transferred into the corona charge density Q_{corona} (Q_c), and Surface Recombination Velocity (SRV, S), respectively.
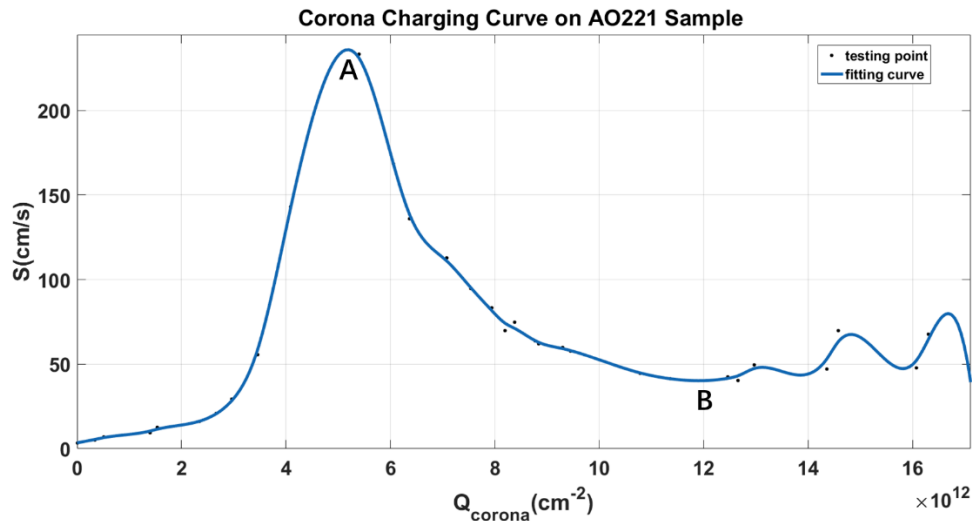
Figure 4-2 Corona Charging Curve of AO221 Sample, with peak point A and overcharge point B

The charging curve of one of the ALD Al_2O_3 samples (AO221) is shown in Figure 4-2. The curve is divided into three regions by point A (peak point of the curve) and point B:

The first region is from starting point to point A. In this region of curve, the corona charges start dropping on the surface, neutralizing the fixed charge inside the Al_2O_3. As the net charge decreasing, the field effect passivation becomes weaker, more minority carriers could move to the surface, as the chemical passivation does not change, more minority carriers recombining at the surface, leading to a decrease of the lifetime of the minority carriers, and an increase of the surface recombination velocity. It could be seen from the Figure 4-2, the SRV changes from nearly 0 to around 235 cm/s.

The second region of the curve is from point A to point B. At point A, all the fixed charge inside Al_2O_3 has been neutralized, with the corona charges continually dropping, the net charge starts to increase, which leads to an opposite result comparing to the first part of the curve. Field-effect passivation becomes stronger, the lifetime starts to increase and the surface recombination velocity starts to decrease, the SRV changes from 235cm/s to 40 cm/s.

The third region is the curve after point B to the end. According to the principle, as more charges dropping on the surface, the lifetime will keep on increasing and SRV will keep on decreasing. However, the SRV starts to rise again. Jin et al. give an explanation to this phenomenon [30], their results show that both positive and negative corona charging either introduce additional interface defects or activates previously deactivated hydrogen passivated defects. The point at which an apparent increase in SRV can be observed as point B in Figure 4-2, which indicates the latest possible onset of the degradation of the surface

33

properties. The onset probably occurs earlier for shorter charging times but is masked by the effect of increasing positive or negative charge, which leads to a decrease in the surface minority carrier concentration and an overall decline in surface recombination.

Here named point A as the peak point, and point B as the overcharge point. At point A, all the fixed charge has been neutralized, which means the corona charge density Q_c value equals to the fixed charge density Q_f value, so the x-axis coordinate of the peak point is the value of the fixed charge density in the testing sample. However, as the fixed charge density has a different polarity, according to Equation 2-1, the fixed charge density of the AO221 sample is -5.19*10^{12}cm^{-2}.

After testing sample AO221, three more samples (AO222, AO223, AO224) manufactured in the same conditions are tested for investigating the exact value of the fixed charge density of the double side polished ALD Al_2O_3 sample, and the result curve is shown in Figure 4-3.
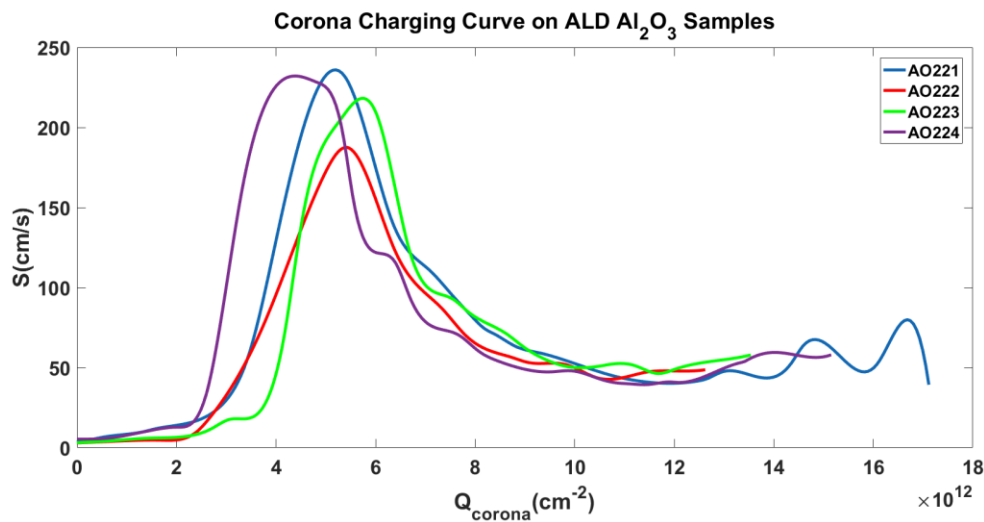
Figure 4-3 Corona Charging Curve on ALD Al_2O_3 Samples (blue: AO221; red:AO222; green:AO223; purple: AO224)

From Figure 4-3, all the curves are in the same shape, and a clear peak point could be found from each curve, the value of the Q_f are shown in Table 4-1.

Table 4-1 Q_f value for different ALD Al_2O_3 samples

Sample	AO221	AO222	AO223	AO224
Q_f (10^{12} cm^{-2})	-5.19	-5.40	-5.75	-4.36

For all the ALD Al_2O_3 samples, their fixed charge densities are all around -5 * 10^{12} cm^{-2}. This value is quite like the value reported from Adam [28], who did the corona charging experiment with the traditional setup on the samples with the same manufacturing process. This result could testify that the DST corona charging system works on its function for the positive corona charging.

4.1.3 Influence of the c-Si Substrate Texture

After testing the double side mirror polished ALD Al_2O_3 samples, some different textured ALD Al_2O_3 samples are fabricated to test the influence of the c-Si texture on the fixed charge density. In real solar cell, especially in some most high-efficiency solar cells have, at least at the front surface, a random-pyramid texture is applied to ensure good light trapping and correspondingly a high short-circuit current density. [11]
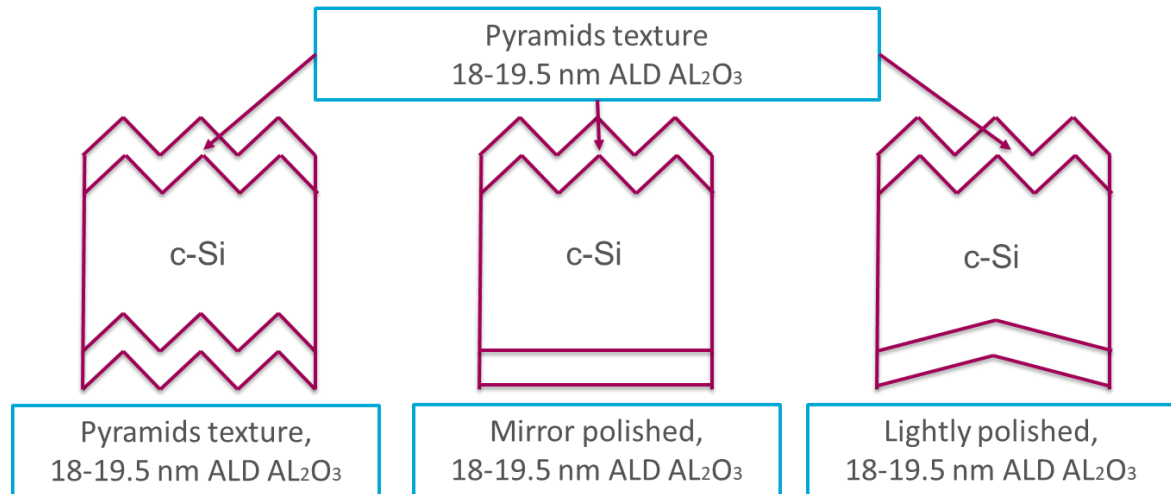
Figure 4-4 Schematic of the ALD Al_2O_3 samples with three different textures, for all three samples the layer thickness is 18-19.5 nm, one side is pyramids texture, the other side is pyramids texture, lightly polished, mirror polished, respectively

According to Figure 4-4, three different samples are prepared, all of them with one side pyramids texture, the other side is pyramids, mirror polished, lightly polished, respectively. The ALD Al_2O_3 layers are made with three passes of 6-6.5nm in each pass, which leads to a total layer thickness around 18-19.5nm, then the wafers are annealed at 600 °C for 20 minutes. Compared to other ALD Al_2O_3 samples tested before, the layer thickness is similar, the only difference comes from the c-Si texture.
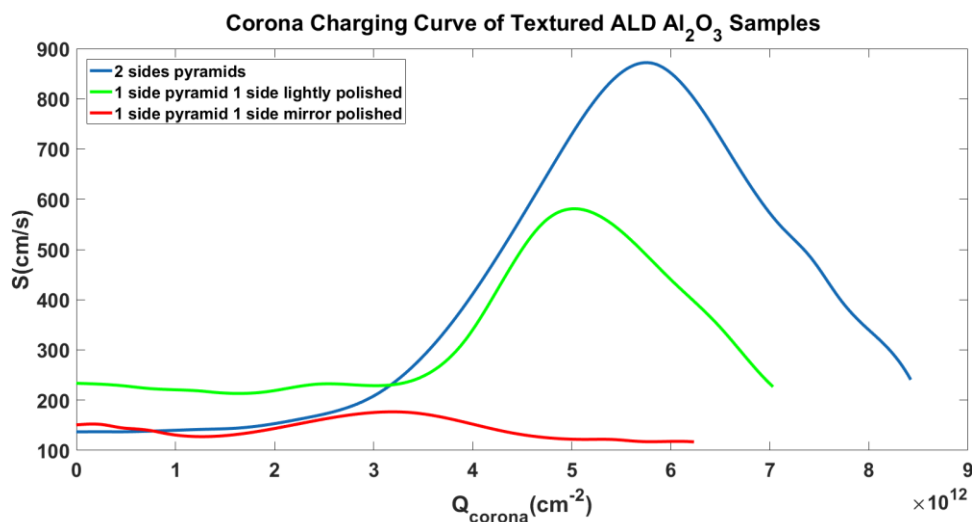
Figure 4-5 Corona Charging Curve of ALD Al_2O_3 Samples (blue: two sides pyramids; green: one side pyramids, one side lightly polished; red: one side pyramids, one side mirror polished)

From Figure 4-5, because of the less polished surface, the starting SRV is relatively low comparing to the double side mirror polished samples. The curves of double side pyramids and one side pyramids one side lightly polished have the same tendency as the double side mirror polished curve, the peak point of the curve could be found easily. However, for the one side pyramids one side mirror polished sample, with the corona charging depositing on top of it, there are not much changes in the surface recombination velocity, there is only a small peak instead of a spike. The testing value of the Q_f is shown in Table 4-2.

Table 4-2 Q_f value for different textured ALD Al_2O_3 samples

Sample	Double Side Pyramids	One Side Pyramids, One Side Lightly Polished	One Side Pyramids, One Side Mirror polished
Q_f (10^{12} cm^{-2})	-5.75	-5.02	-3.19

For their fixed charge density value, except the one side pyramids and one side mirror polished, the other two values are close to the value of double side mirror polished sample. It shows that the c-Si texture does not influence the fixed charge density. The difference of the one side pyramids one side mirror polished may cause by the unsymmetrical structure. The pyramids texture typically results in an increase of roughly ~1.7 in surface recombination for Al_2O_3-based passivation schemes compared to planar surfaces, which can be attributed to the increase in surface area [11]. As the difference does not influence the fixed charge density (comparing the Q_f result from double side pyramids and double side mirror polished). If the surface area increases 1.7 times, the total amount charge on a certain surface also increases 1.7 times. As the corona charging speed does not change, this will lead to a difference in the charging time.
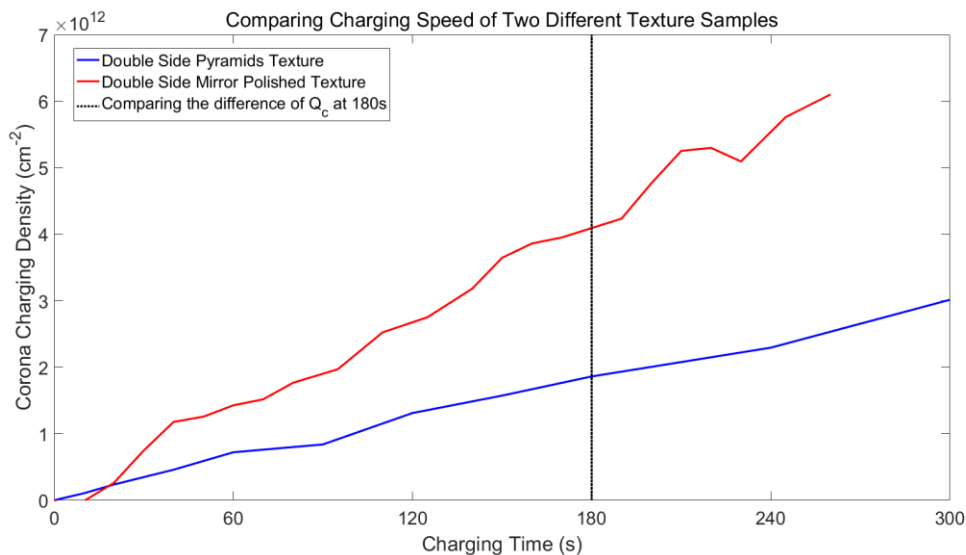

Figure 4-6 Charging Time of the Two Different Texture Samples (red: double sides mirror polished; blue: double sides pyramids texture), the black line shows the difference when both samples charged for 180 seconds, the charge density of double side mirror polished sample is 2.35 times the pyramids texture sample

As it is shown in Figure 4-6, the x-axis is the charging time, the y-axis is the Q_c, and it clearly shows that the mirror polished sample has a higher corona charge density increasing speed than the pyramids texture sample. If there is the same amount of corona charges deposited on the Al_2O_3 layer, as the pyramids sample surface area is bigger than the mirror polished sample, so the corona charge density for the pyramids sample is smaller, to reach the same level of corona charge density, more corona charges needs to be dropped on the surface, which requires a longer charging time for the pyramids texture sample. In principle, the value depends on the surface area difference which is 1.7. However, from the experimental result, the difference in charging time is 2.35. Some other issues may also influence the value.

This could explain the result of the one side pyramids one side mirror polished sample. For both sides of the wafer charged for the equal amount of time, same amount of corona charges drops on the surface, but due to the difference in surface area, the corona charge density is different. When one side fixed charge density is all nullified, the other side still has negative fixed charge density, the carrier lifetime does not drop significantly. When the other side fixed charges are nullified, there are more positive corona charge density appears on the former side to enhance the passivation. That makes the one side pyramids one side mirror polished sample hard to find the spike in the charging curve.

For the one side pyramids one side lightly polished sample, the difference of the surface area is between 1 and 1.7, which may cause less effect on testing the fixed charge density, making the sample able to find the spike of the charging curve.

4.2   Corona Charging on PECVD SiN_x

4.2.1   Sample Preparation

As the system is suitable for material with negative fixed charge density, besides the negative fixed charge density material, there is positive fixed charge material applied for n+ c-Si material passivation. Silicon Nitride (SiN_x) films provide excellent surface passivation, on the one hand, due to the presence of fixed positive charges the field-effect passivation exists; on the other hand, due to the large percentage of atomic hydrogen, it also has a good chemical passivation property. Lauinger et al. reported record low surface recombination velocity value of 4 cm/s on remote-plasma SiNx coated low-doped FZ p-Si samples [32].
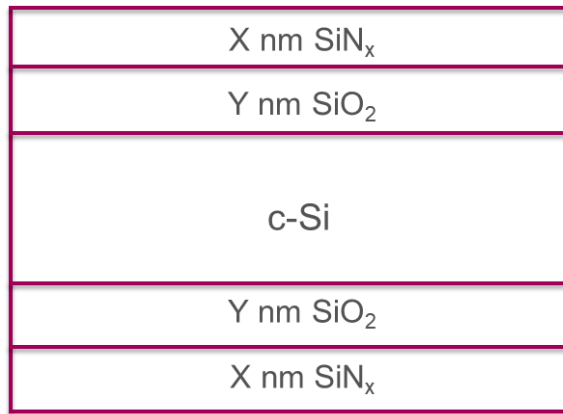
X nm SiN$_x$
Y nm SiO$_2$
c-Si
Y nm SiO$_2$
X nm SiN$_x$

Figure 4-7 Schematic of the Silicon Nitride Sample, Y cm thickness SiO$_2$ layer is deposited on the low-doped, n-type c-Si bulk, then X cm PECVD SiN$_x$ is deposited above SiO$_2$ layer, X, Y value are shown in Table 4-3

The schematic of the SiNx samples all shown in Figure 4-7, the c-Si bulk is the same as the ALD Al$_2$O$_3$ samples, the SiO$_2$ is thermally grown on top of the c-Si bulk, the SiN$_x$ is deposited on the top of the SiO$_2$ through PECVD process. X, Y is the thickness of SiN$_x$ and SiO$_2$ respectively, there are various combinations of the X, Y to create different SiN$_x$ samples, which is shown in Table 4-3.

Table 4-3 Different thickness of the SiN$_x$ and SiO$_2$ layers

X(cm) ╲ Y(cm)	40	70	100
0	(0,40)	(0,70)	(0,100)
1.5	(1.5,40)	(1.5,70)	(1.5,100)
10	(1.5,40)	(10,70)	(10,100)

Taking different X, Y values, there are nine combinations of layer thickness.

4.2.2 **Experimental Result**

For the SiO$_2$ thickness Y=0 cm or Y=1.5 cm, when doing the corona charging process, the surface voltage tested by the Kelvin Probe does not change during the whole process, which means there are no corona charges deposited on the top of the SiN$_x$ layer. It means that in corona charging curve the x-axis value does not change during the whole process. This situation may due to the leakage of the SiN$_x$ layer, as the layer is more conductive compared to other dielectric layers, the charge may drop on the surface and then go to the ground through the bulk.

This phenomenon is changed with the Y=10 cm layer, according to V. Sharma [33], the thin thermal oxide film (~18 nm) underneath the nitride film acted as a perfect charge blocking layer, preventing any charge movement between the silicon substrate and the nitride film. For the Y= 10 cm samples, their charging curves could be tested.
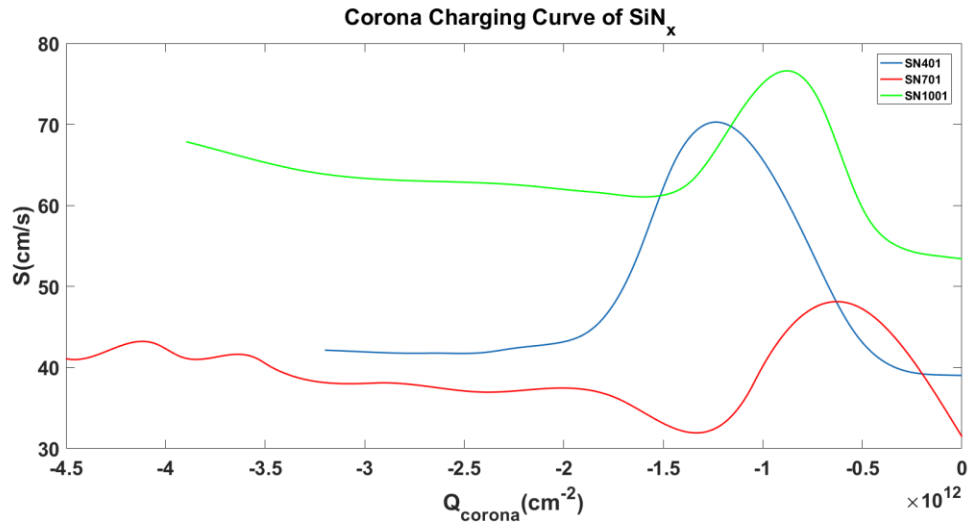
Figure 4-8 Corona Charging Curve of PECVD SiN_x (blue: SN401; red:SN701; green: SN1001)

The charging curve of PECVD SiN_x is shown in Figure 4-8, SN401, SN701, SN1001, represent the 40nm, 70nm, 100nm layer thickness of the SiN_x layer. Compared to the ALD Al_2O_3 charging curves, this time the corona charge density is negative as there are positive fixed charges inside the SiN_x layer, the overcharge point could still be observed. The Q_f value is smaller than the ALD Al_2O_3 samples. The result is shown in Table 4-4.

Table 4-4 Q_f value for different thickness PECVD SiN_x samples

Sample	SN401	SN701	SN1001
Q_f (10^{12} cm^{-2})	1.24	0.63	0.88

According to Table 4-4, For different layer thickness, the fixed charges density is also a little bit different, all the result is around $1 * 10^{12}$ cm^{-2}. Compared to the result shown in Figure 1-3, the result is similar. Proving that the newly developed system also works for the material contains positive fixed charges.

4.3 Corona Charging on LPCVD poly-Si

4.3.1 Sample Preparation

The usage of ion-implanted poly-Si as potential passivating contacts for c-Si solar cells has been recently reported, it provides excellent passivation quality also a lean process. [34,35]

The poly-Si layers are deposited on the bare silicon wafer at 580 °C by Low Pressure Chemical Vapor Deposition (LPCVD) with a thickness of 250 nm. Boron and phosphorous dopants are locally ion-implanted into the poly-Si to created different doping. A subsequent high temperature annealing, at 950 °C for 5 minutes, is used to activate and drive in both types of dopants. Leading to the p++ poly-Si layer (active charge density is $1*10^{20}$ cm^{-3}), n++ poly-Si layer (active charge density is $2*10^{20}$ cm^{-3}). [36] The schematic is shown in Figure 4-9 (a).
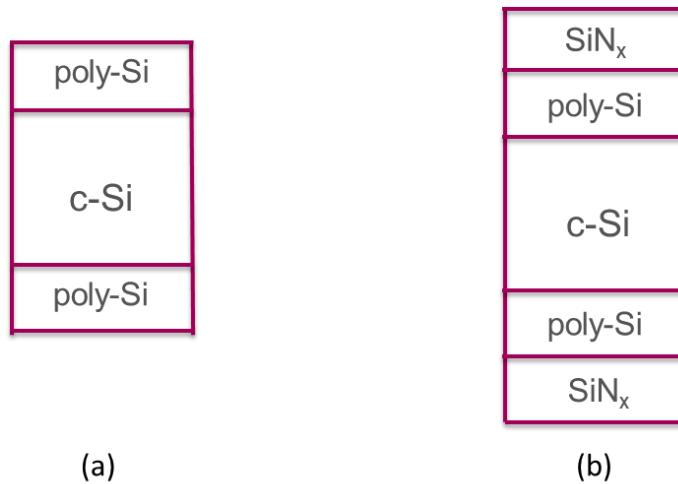
Figure 4-9 Schematic of the poly-Si sample (a) two 250nm highly-doped poly-Si layers are deposited on the low-doped n-type c-Si bulk respectively, one is n-type poly-Si, the other is p-type; (b) after the process in (a), 80nm PECVD SiN_x capping layers are deposited on half of the each sample, then each sample is cut in half to create four different samples

After the process of the sample in Figure 4-9 (a), two 80nm thickness of the PECVD SiN_x layers are deposited on both side of the sample as the capping layer, the schematic of this sample is shown in Figure 4-9 (b). In total, there are four samples: p++ poly-Si without capping layer; n++ poly-Si without capping layer; p++ poly-Si with capping layer; n++ poly-Si with capping layer.

4.3.2 Experimental Result

Same as the thin oxide layer thickness PECVD SiN_x sample, both poly-Si samples without the capping layer are quite leaky, it is not able to deposit stable corona charges on the surface of the samples. For the samples with capping layer, they could be charged, the charging curves are shown in Figure 4-10. As the bare poly-Si sample could not be charged, it indicates that the corona charges are located on the SiN_x capping layer.

Figure 4-10 corona charging curve of the n++/p++ LPCVD poly-Si (red: n++ poly-Si with negative corona charging; blue: n++ poly-Si with positive corona charging; green: p++ poly-Si with negative corona charging; pink: p++ poly-Si with positive corona charging)

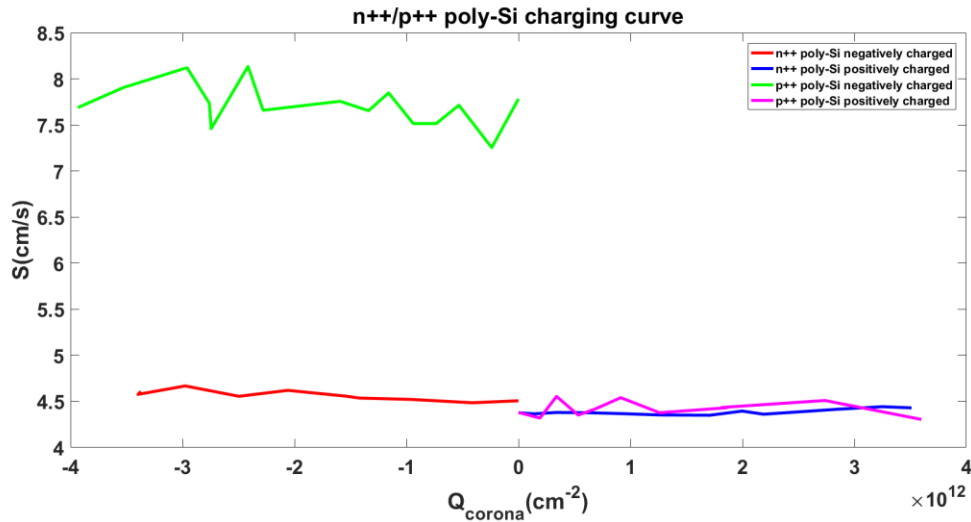According to Figure 4-10, the samples are both positively and negatively charged. Among the four charging curves, none of them follows the shape of the ALD Al_2O_3 or PECVD SiN_x. No peak point could be found through the entire curve.

For no peak point could be found, there are two main reasons for this. Firstly, the corona charges comparing to the doping density differences between the poly-Si and c-Si is relatively low. As the active doping density is $1*10^{20}$ cm^{-3}, times the layer thickness of the poly-Si, the fixed charge density inside the poly-Si is much higher than the corona charge density dropping on the SiN_x, which makes the corona charges not effective in influence the surface recombination. Secondly, the large thickness of the poly-Si weakens the field effect of the fixed charges in the SiN_x. As the thickness of poly-Si layer is 250nm, the PECVD SiN_x is 80nm, the distance between the corona charges and the c-Si surface is 330nm, comparing to 50-110 nm in PECVD SiN_x samples and around 20nm in ALD Al_2O_3 samples. The field create by one single charge is decreasing with the increasing of the distance to the charge. The long distance may weaken the field of the corona charge to make it less effective. So, for current poly-Si sample structure, the corona setting is not able to test the fixed charge or even change the carrier lifetime of the poly-Si samples.

5 Decay of the Corona Charge Density

5.1 Sample Preparation

According to the experiment result of thinner oxide layer thickness PECVD SiN_x and LPCVD poly-Si without capping layer, the leakage happens when using corona charging on the samples. The leakage could be treated as the fast decay of corona charges, as the surface charges generated by corona charging disappear so fast which is not able to test the value.

The same phenomenon may also happen with the samples that could be charged. The corona charges may just stay on the sample longer than the samples which cannot be charged, for example, for the ALD Al_2O_3 sample according to B.M.H. van der Loo [11], the charge may stay for weeks. There will also have charge decaying happens for a long-time scale, but it just will not influence the testing process.

Three kinds of charged samples are prepared for decay testing, which is shown in Figure 5-1.
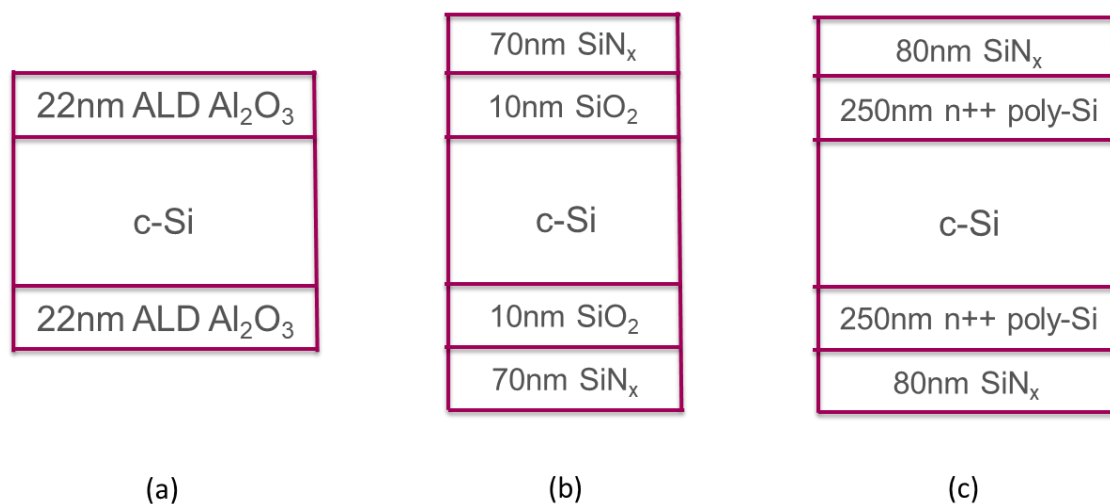
Figure 5-1 Samples for decay testing, (a) is the same sample in Chapter 4.1; (b) is the sample in Chapter 4.2 with thermally grown SiO_2 thickness X=10 nm, PECVD SiN_x thickness Y=70nm; (c) is the n++ sample with the PECVD SiN_x capping in Chapter 4.3

All the samples have been charged to the end of their corona charging curves. For testing the fixed charge density value, the ALD Al_2O_3 has been positively charged, and the PECVD SiN_x

42

sample has been negatively charged. For the n++ poly-Si sample, both positively and negatively charged samples are prepared for the test.

5.2   System Settings for Decay Measurement

The function for testing decay has been mentioned in Chapter 2.4. As the system has a two seconds delay after the corona charging, then one to three seconds to move the holder from the corona charging area to the Kelvin Probe, for the first five seconds, the system is not able track the decay. For thinner oxide layer thickness PECVD SiN_x and LPCVD poly-Si without capping layer, the charge may decay within five seconds, so that there is no surface voltage change measured by Kelvin probe, which is also not suitable for the decay testing. For other three prepared samples, they have shown a clear value by Kelvin probe during the fixed charge measurement, so the charge will not decay in this short duration.

To track the decay curve, a ten seconds time step has been set to draw the curve precisely, the total tracking time is 24 hours to see the whole charges decaying curve.

5.3   Decay Curves of Different Materials

The original data of the decay curves are shown in Figure 5-2.
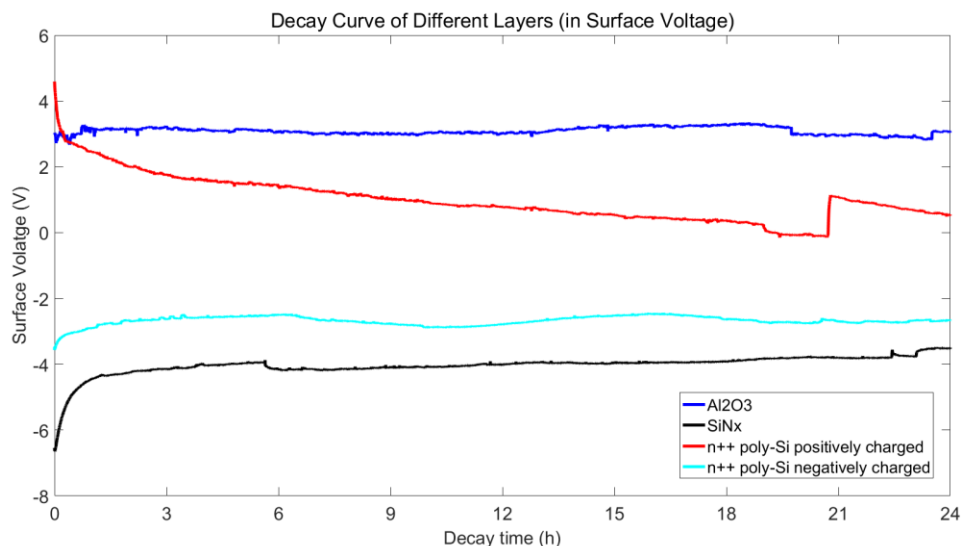
Figure 5-2 Decay curve of different layers (blue: ALD Al_2O_3 sample positively charged; black: PECVD SiN_x negatively charged; red: n++ poly-Si positively charged; cyan: n++ poly-Si negatively charged, all data shown in surface voltage)

From Figure 5-2, only ALD Al_2O_3 sample has a stable curve, which means the charge could stay on the surface for more than 24 hours. Other materials all experience some extent of decay. Most of the fast decaying happens in the first three hours, as most of the wafers are overcharged, it stays in an unstable status, the excess charges decay to make the sample back

to the stable status. After three hours for both negatively charged n++ poly-Si and PECVD SiN$_x$ has a quite stable curve; for the positively charged n++ poly-Si goes on decaying, at around 21 hours, it drops all the corona charges, then a sudden peak appears, this may be caused by some human interaction issues.

However, as the initial surface voltage is different, using the surface voltage is hard to describe their decaying properties clearly, so all the value has been normalized (dividing each initial surface voltage value) to show their decay percentage, which is shown in Figure 5-3.
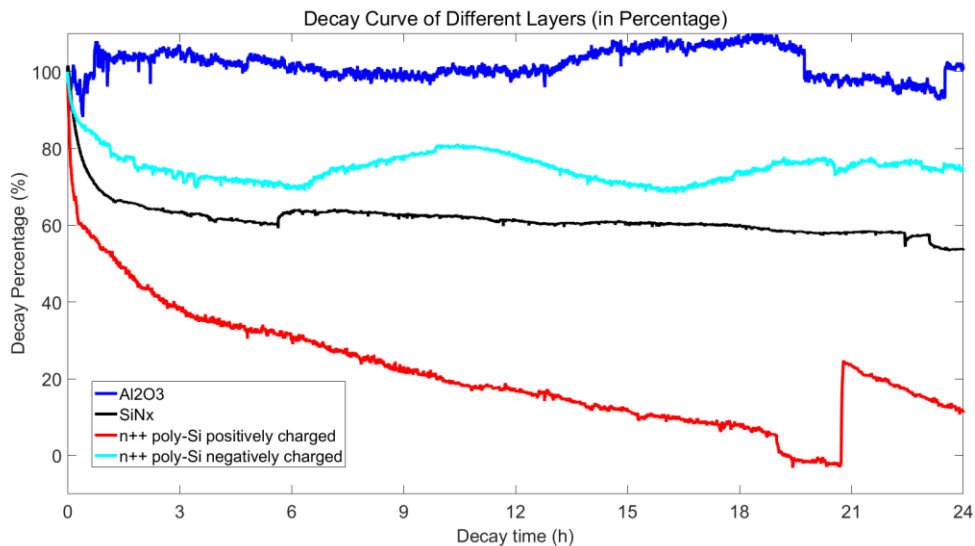
Figure 5-3 Decay curve of different layers (same data as Figure 5-2, shown in percentage)

According to Figure 5-3, The decay properties are shown more intuitively, and several conclusions could be drawn:

ALD Al$_2$O$_3$ has a stable curve, as there is almost no decline during the whole process.

Comparing PECVD SiN$_x$ and negatively charged n++ poly-Si, their decaying curves are quite similar, considering there is a PECVD SiN$_x$ capping layer outside the poly-Si, both decaying happens on the same material with the same charge polarity. The difference may due to the poly-Si between the PECVD SiN$_x$ and the c-Si.

Comparing the positively charged n++ poly-Si and the negatively charged n++ poly-Si, the positively charged sample decays faster than the negatively charged one. As there are positively fixed charge density in PECVD SiN$_x$ capping layer, this fixed charge will repel the positive corona charges as there are in the same polarity, which makes the positive corona charges in a more unstable status and makes them easier to decay.

6 Conclusion and Future Work

6.1 Conclusion

In order to increase the efficiency of the solar cell, reducing the surface recombination is one of the most important tasks. Passivating layers are applied as it will offer both chemical passivation and field-effect passivation. It is vital to determine the amount of passivation provided by each passivation principle. They are indicated by two parameters: density of the interface traps D_{it} for chemical passivation and fixed charge density Q_f for field-effect passivation.

To determine the field-effect passivation, a corona charging system from DST had been newly developed. To improve various features of the system, some different methods of the lifetime testing have been studied, and then some new functions have been added to the system.

Among those features, one of the most important features is the charge uniformity. With uniformly distributed charges, the measurement result should become more precise. Single needle system, multiple needles system, single needle mesh system, and rotation charging system have been developed. Each of these systems has its own advantages and disadvantages. Single needle system has the worst uniformity but is easy to build; multiple needle system performs better, but the inception voltage becomes higher; single needle mesh system shows good uniformity only in a small area; rotation charging system has the best uniformity, but more components are required to build the system.

Several samples' fixed charge densities have been tested by the system to check whether the system works appropriately. For ALD Al_2O_3 sample, with positive corona charging, the fixed charge density is around $-5 * 10^{12}$ cm^{-2}; for PECVD SiN_x sample, with negative corona charging, the fixed charge density is around $+1 * 10^{12}$ cm^{-2}. Both results are consistent with the previous results done by other research institutes. Besides, poly-Si, a newly developed material is tested by the corona charging system, showing that it can only be charged with a PECVD SiN_x capping layer. Even with the capping layer, no matter switching the doping polarity of poly-Si or the corona charging polarity, the corona surface charges do not influence the passivation on the c-Si surface. Besides, during the corona charging experiment, some materials present

quite leaky. No corona charges stayed on the surface as the layers are quite conductive, which is not suitable for the corona charging system.

The influence of different textures of the c-Si bulk on fixed charge density was studied. Three kinds of samples, namely double sides pyramids, one side pyramids one side lightly polished, one side pyramids one side mirror polished are measured to compare to the traditional double sides mirror polished ALD Al_2O_3 sample. According to the result, the texture does not influence the fixed charge density, as the double sides pyramids sample has same amount of charge as the double sides mirror polished sample. However, for the pyramids textured surface, it may take longer to charge it compared to the mirror polished one. Due to this issue, the unsymmetrical sample is not able to be tested with traditional testing method since charging the same period will cause a different corona charge density on different side of the wafer.

In the end, the decay properties of different materials have been tested, where all the samples stayed under the Kelvin probe for 24 hours after the corona charging experiment. According to the decay curve, for ALD Al_2O_3, the corona charges are quite stable on the surface, as the charge density is similar to the value before the decay measurement; for PECVD SiN_x and the poly-Si with a PECVD SiN_x capping layer, the corona charge density decreases in 24 hours. The most severe decay happens on the poly-Si with a PECVD SiN_x capping layer using positive corona charging.

6.2   Future Work

During the master thesis project, some issues can be potentially improved. Thus, future work is suggested focusing on dealing with these following problems.

1.   Lifetime tester integrating

As for now, carrier lifetime is tested by the Sinton machine outside of the corona charging box. To build an automatic system that the whole process is controlled by the software, it is important to integrate the lifetime tester into the Corona Charging System. As several lifetime testing methods have been studied. The final method can be decided in the future, and a mounted plan can also be carried out.

2.   Testing the real rotation charging system

Due to certain issues, the rotation charging system has not been manufactured, so the system has been simulated by using same needle charging in each position. As in the real system, the rotation may influence the charge distribution, which may lead to a different result. Besides, it remains to be studied that how to make the system rotate properly.

3.   Corona charging on LPCVD poly-Si

Chapter 4.3 shows that it is only able to charge the poly-Si with a capping layer. However, this charge did not work because of the high doping density and the large thickness of the poly-Si.

A new test can be carried out with lower doped poly-Si and thinner poly-Si layer, to study which issue is more important for weakening the effect of the surface charge.

4. Decay Measurement control

From Figure 5-3, large fluctuation can be found for every decay curve. There even appears some spikes in ALD Al_2O_3 and n++ poly-Si positively charged curves. As the decay testing function is newly added to the system, the testing method and the environment control could be further improved in various aspects, such as controlling humidity, illumination etc.

7 Reference

[1]. Schellnhuber, Hans-Joachim. World in transition: Towards sustainable energy systems. Vol. 3. Earthscan, 2004.

[2]. Europe, Solar Power. "Global Market Outlook for Solar Power/2017–2021." Solar Power Europe: Bruxelles, Belgium (2017): 32.

[3]. E. Becquerel, Comptes Rendus 9, 561 (1839).

[4]. Chapin, D.M., Fuller, C.S., and Pearson, G.L. (1954) A New Silicon p-n Junction Photocell for Converting Solar Radiation into Electrical Power. J. Appl. Phys., 25 (5), 676.

[5]. K. Yoshikawa, "Exceeding Conversion Efficiency of 26% by Silicon Heterojunction Technology," presented at the 7th Silicon PV Conf. April 2017 (2017)

[6]. J. G. Fossum and E. L. Burgess, "High-efficiency p+-n-n+ back-surface-field silicon solar cells," Applied Physics Letters, vol. 33, pp. 238-240, 1978.

[7]. Cuevas, A. et al. Skin care for healthy silicon solar cells. in 2015 IEEE 42nd Photovoltaic Specialist Conference (PVSC) 1–6 (IEEE, 2015). doi:10.1109/PVSC.2015.7356379

[8]. G. Groeseneken, H. E. Maes, N. Beltran, and R. F. de Keersmaecker, "A reliable approach to charge-pumping measurements in MOS transistors," IEEE Trans. Electron Devices, vol. ED-31, no. 1, pp. 42–53, Jan. 1984.

[9]. Glunz, S. W., et al. "Field-effect passivation of the SiO2 Si interface." Journal of Applied Physics 86.1 (1999): 683-691.

[10]. S. Dauwe, Ph.D. thesis, Hannover University, 2004

[11]. van der Loo B.W.H, Ph.D. thesis, TU Edinhoven, 2017

[12]. Lord Kelvin, Philos. Mag. 46, 82 (1898)

[13]. Sinton, R. A., and T. Mankad. "Contactless carrier-lifetime measurement in silicon wafers, ingots, and blocks." Measurement (2009): 1-14.

[14]. Sinton, Ronald A., Andres Cuevas, and Michael Stuckings. "Quasi-steady-state photoconductance, a new method for solar cell material and device characterization." Photovoltaic Specialists Conference, 1996., Conference Record of the Twenty Fifth IEEE. IEEE, 1996.

[15]. Burtscher, J., F. Dannhäuser, and J. Krausse. "Die Rekombination in Thyristoren und Gleichrichtern aus Silizium: ihr Einfluss auf die Durchlasskennlinie und das Freiwerdezeitverhalten." Solid-State Electronics 18.1 (1975): 35-63.

[16]. Wilson, Marshall, et al. QSS-μPCD measurement of lifetime in silicon wafers: advantages and new applications. Energy Procedia 8 :128-134. (2011)

[17]. ZHOU, Chun-lan, and Wen-jing WANG. "Lifetime measurement for minority carrier of crystalline silicon solar cells [J]." China Measurement Technology 6.6 (2007): 25-31.

[18]. Jones, J. E. "A theoretical explanation of the laws of Warburg and Sigmond." Proceedings of the Royal Society of London A: Mathematical, Physical and Engineering Sciences. Vol. 453. No. 1960. The Royal Society, 1997.

[19]. Warburg E 1927 Characteristik des spitzenstromes Handbuch der physik (Berlin: Springer)

[20]. Allibone T E and Saunderson J C 1989 Corona at very high direct voltages. V. Corona in rod/plane gaps 6th Int. Symp. on high voltage Engineering (ISH) (New Orleans, LA) Paper 22.02

[21]. Goldman A, Goldman M and Jones J E 1992 On the behaviour of the planar current-distribution in the pulseless regime of negative DC point plane coronas in air Proc. 10th Int. Conf. on Gas Discharges and Applications (GD 92) (Swansea, Wales, UK) pp 270–3

[22]. Bonilla, Ruy S., Frederick Woodcock, and Peter R. Wilshaw. "Very low surface recombination velocity in n-type c-Si using extrinsic field effect passivation." Journal of Applied Physics 116.5 (2014): 054102.

[23]. Jones, James Edward. "On the interaction of adjacent coronae: a description of the electric field behaviour on the planar line beneath twin coronating negative DC points in air." IEE Proceedings-Science, Measurement and Technology 153.2 (2006): 81-92.

[24]. Jaworek, A., and A. Krupa. "Electrical characteristics of a corona discharge reactor of multipoint-to-plane geometry." Czechoslovak Journal of Physics 45.12 (1995): 1035-1047.

[25]. Moreno, R. A., and B. Gross. "Measurement of potential buildup and decay, surface charge density, and charging currents of corona‐charged polymer foil electrets." Journal of applied physics 47.8 (1976): 3397-3402.

[26]. Mandoc, M. M., et al. "Corona charging and optical second-harmonic generation studies of the field-effect passivation of c-SI by Al 2 O 3 films." Photovoltaic Specialists Conference (PVSC), 2010 35th IEEE. IEEE, 2010.

[27]. Giacometti, Jose A., and Osvaldo N. Oliveira. "Corona charging of polymers." IEEE Transactions on Electrical Insulation 27.5 (1992): 924-943.

[28]. Adams, M. L. C. "Silicon surface passivation by thin films studied by corona charging." (2011).

[29]. Richter, A., Benick, J., Kimmerle, A., Hermle, M. & Glunz, S. W. Passivation of phosphorus diffused silicon surfaces with Al2O3: Influence of surface doping concentration and thermal activation treatments. J. Appl. Phys. 116, 243501 (2014).

[30]. Jin, Hao, et al. "Defect generation at the Si–SiO2 interface following corona charging." Applied physics letters 90.26 (2007): 262109.

[31]. T. Lauinger, J. Schmidt, A.G. Aberle, R. Hezel, "Record low surface recombination velocities on 1 Ω cm p-silicon using remote plasma silicon nitride passivation," Applied Physics Letters, vol. 68, issue 9, pp. 1232-1234, 1996

[32]. Sharma, Vivek. Study of charges present in silicon nitride thin films and their effect on silicon solar cell efficiencies. Arizona State University, 2013.

[33]. U. R€omer, R. Peibst, T. Ohrdes, B. Lim, J. Kr€ugener, T. Wietler, and R. Brendel, IEEE J. Photovoltaics 5(2), 507 (2015). 8

[34]. D. L. Young, W. Nemeth, V. LaSalvia, R. Reedy, S. Essig, N. Bateman, and P. Stradins, IEEE J. Photovoltaics 6, 41 (2015).

[35]. Yang, Guangtao, et al. "Design and application of ion-implanted polySi passivating contacts for interdigitated back contact c-Si solar cells." Applied Physics Letters 108.3 (2016): 033903.

8 Appendix

8.1 Control Software

The corona charging system is controlled by a special software designed for its function, and the current version is v1.05, the software interface is shown in Figure 8-1.
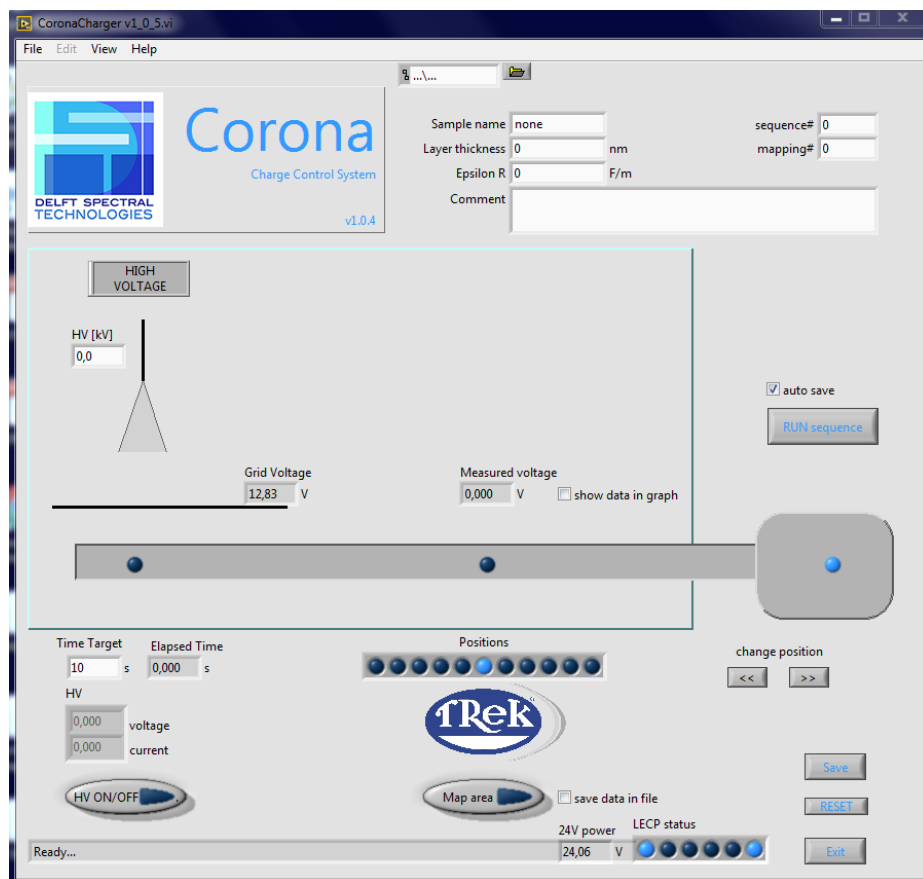

Figure 8-1 Corona Charging Control interface (v1.05)

From the top, the features of the sample (name, layer thickness, relative permittivity) need to be filled in, on the right side, it could also indicate how many sequences user has run so far. Three positions for the holder could be seen on the interface, and the holder could be moved by pressing the 'change position' buttons. For testing the surface voltage of the sample, the

software allows a maximum 11 positions mapping on the sample, and users could choose which position they would like to test by pressing the points under 'positions', then press 'map area' to test all the selected points. The voltage setting is on the left side, here the charging time and charging voltage could be set, during charging, the charging status will show under the 'HV', with voltage in kV and current in μA. Besides the traditional charging function, the system could track the charges decay on the sample surface by placing the sample under the Kelvin probe then tick the box of 'show data in graph'. Then fill in the tracking time step via the pop-up, then the surface voltage change will be tracked by the Kelvin probe and save the data in file for future applications.